Non-invasive Imaging of Retinal degeneration in Small Animals Using Fourier Domain Optical Coherence Tomography

By

Jing Xu
B.Eng, Yangzhou University, 2005

THESIS SUBMITTED IN PARTIAL FULFILLMENT OF
THE REQUIREMENTS FOR THE DEGREE OF

MASTER OF APPLIED SCIENCE

In the
School
of
Engineering Science

SIMON FRASER UNIVERSITY

Fall 2009

APPROVAL

Name: **Jing Xu**

Degree: **Master of Applied Science**

Title of Thesis: **Non-invasive Imaging of Retinal Degeneration in Small Animals Using Fourier Domain Optical Coherence Tomography**

Examining Committee:

Chair: Dr. Shahram Payandeh, P.Eng.
Professor, School of Engineering Science

_____
Dr. Marinko V. Sarunic
Senior Supervisor
Assistant Professor, School of Engineering Science

_____
Dr. Glenn H. Chapman, P. Eng.
Supervisor
Professor, School of Engineering Science

_____
Dr. Mirza Faisal Beg, P. Eng.
Internal Examiner
Associate Professor, School of Engineering Science

Date Defended/Approved: December 22, 2009

ABSTRACT

A prototype spectrometer based on Fourier Domain Optical Coherence Tomography (FD OCT) system was used as a non-invasive depth resolved medical imaging tool for diagnostic visualization of the retinal structures *in vivo*. This thesis investigated so-called Spectral Domain (SD) OCT to detect and monitor pathological signs of retinal degeneration in small animals such as mice, rats and *Xenopus laevis* larvae. Non-invasive SD OCT imaging was validated against invasive retinal cross sectional images (histology) acquired from a nearby region for comparison of specific retinal layers. The retinal layers were manually segmented for quantitative thickness measurements, and followed by statistical analysis to determine the onset of detectable retinal degeneration. The results of this research have demonstrated that FD OCT is a powerful tool for quantitative *in vivo* measurement of retinal degeneration in small animals.

Keywords: optical coherence tomography, retinal degeneration, small animal imaging

Declaration of Partial Copyright Licence

STATEMENT OF ETHICS APPROVAL

The author, whose name appears on the title page of this work, has obtained, for the research described in this work, either:

(a) Human research ethics approval from the Simon Fraser University Office of Research Ethics,

or

(b) Advance approval of the animal care protocol from the University Animal Care Committee of Simon Fraser University;

or has conducted the research

(c) as a co-investigator, collaborator or research assistant in a research project approved in advance,

or

(d) as a member of a course approved in advance for minimal risk human research, by the Office of Research Ethics.

A copy of the approval letter has been filed at the Theses Office of the University Library at the time of submission of this thesis or project.

The original application for approval and letter of approval are filed with the relevant offices. Inquiries may be directed to those authorities.

Simon Fraser University Library
Simon Fraser University
Burnaby, BC, Canada

Last update: Spring 2010

ACKNOWLEDGEMENTS

I would like to express my deepest gratitude to Dr. Marinko Sarunic for providing me with the opportunity to work on this project in his lab, for continuous guidance, encouragement, support and patience in the progression of my work during my graduate study, and for sharing his passion in the work that he does.

I would like to thank my committee members Dr. Faisal Beg for equipping me with knowledge on image processing and Dr. Glenn Chapman for strengthening my background in lasers.

I would also like to thank the Biomedical Optics Research Group; Mei Young for the help on image acquisition and measurement analysis, Sieun Lee for sharing her experience in using Amira, and Azadeh Yazdanpanah for implementing the semi-auto segmentation algorithm.

Last but not least, I would like to thank my parents for their continued support in all my endeavours.

TABLE OF CONTENTS

LIST OF FIGURES

LIST OF TABLES

LIST OF ACRONYMS

ANSI	American National Standards Institute
FD	Fourier Domain
FWHM	Full Width Half Maximum
GCL	Ganglion Cell Layer
INL	Inner Nuclear Layer
IOP	Intra-Ocular Pressure
IPL	Inner Plexiform Layer
IS	Inner Segment
NFL	Nerve Fiber Layer
OCT	Optical Coherence Tomography
O.C.T.	Optimal Cutting Temperature
ONH	Optic Nerve Head
ONL	Outer Nuclear Layer
OPL	Outer Plexiform Layer
OS	Outer Segment
RGC	Retinal Ganglion Cell
RPE	Retinal Pigment Epithelium
SD	Spectral Domain
SS	Swept Source
TD	Time Domain

1. INTRODUCTION

1.1 Research Motivation

The visual system in humans offers sharp image clarity and vivid colours. A simple schematic of the human eye is presented in Figure 1-1. The curved surface of the cornea focuses the light, the iris acts as a shutter which opens and closes to let the right amount of light into the eye, and the adjustable shape of the crystalline lens provides accommodation for different distances. The retina is the light sensitive membrane at the back of the eye which is like the film in a camera. It visually captures all the moments of our life that influence our emotions and mind. However, millions of people worldwide are suffering various degrees of vision loss which significantly impacts the quality of their life. Retinal degenerative diseases, such as genetic retinal diseases and age-related macular degeneration, are one of the leading causes of vision loss in the Western world.

Scientists have been investigating causes of retinal diseases and are developing novel therapeutic approaches such as gene therapy to reverse vision loss. Research on ocular diseases is limited by the constraints of studying

pathophysiologic processes in the human eye. Small animal models of ocular diseases provide powerful tools for analysis and characterization of disease pathogenesis and response to treatment.

In order to identify the microstructures of the retina, visual scientists need to enucleate (cut out) the eye for histology. This requires euthanizing the animals, and thus provides data at only a single time point to characterise disease progression or evaluate the effects of therapy. Therefore, non-invasive retinal imaging techniques need to be introduced in order to conduct longitudinal studies and decrease the number of animal models being sacrificed for histology [13]. The challenge to non-invasive imaging is the location of the retina at the back the eye, and the high resolution required to visualize the microstructure of the retinal layers.

1.2 The Eye and the Retina

Generally, the mammalian eye consists of the anterior and posterior segments contained the focusing and detecting elements. Figure 1-1 presents a simple schematic of the human eye.

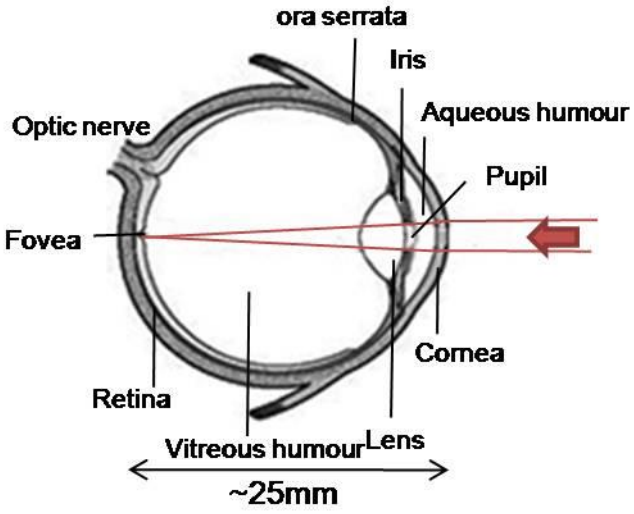

Figure 1-1: Schematic of the human eye. A collimated beam incident on the eye is focused by the cornea and lens onto retina into a sharp point. Modified from National Eye Institute, National Institutes of Health Ref#: NEA09.

The eye is roughly about 25mm in diameter and has many specialized structures and tissues [10]. Light travels through the cornea, pupil, lens, and the image is focused onto the retina at the back of the eye. The majority of the refraction occurs at the cornea, and the shape of the soft lens adjusts the focus from near to far using muscles inside the eye. A circular field of approximately 6mm around the fovea is considered the central retina while beyond this is peripheral retina stretching to the ora serrata, 21 mm from the center of the optic disc. The total human retina is a circular disc of approximately 42 mm diameter [11][12][13]. The retina is approximately 0.5 mm thick, and contains cell layers,

which detect light, perform some processing on the information, and transmits it to the brain via the neurons of the optic nerve.

1.3 The Eye in Small Animals

Small animal like rats, mice and tadpoles have been widely used in ophthalmic research for the purpose of investigating retinal degenerative diseases and to evaluate possible treatments. The small size of the eye creates challenges for non-invasive imaging, with particular details relevant for each different type of laboratory animal.

1.3.1 Rodent Eye

The rodent's eye has similar basic structure and function as the human eye, except for being much smaller.

Figure 1-2 shows a schematic of a mouse or rat eye. The mouse eye has a diameter of only 3-4 mm, and its retinal thickness is about 230μm. The rat eye is similar to the mouse eye in structure, and the retinal thickness is similar (+-10μm) while the rest of the eye differs mainly in scale (about 2 times bigger in diameter). The most visible difference relative to the human eye is the size of the lens, which is proportionately quite large, rounded, and occupies about 75% of

the intraocular space. The visual acuity of the rodents is much worse than humans.

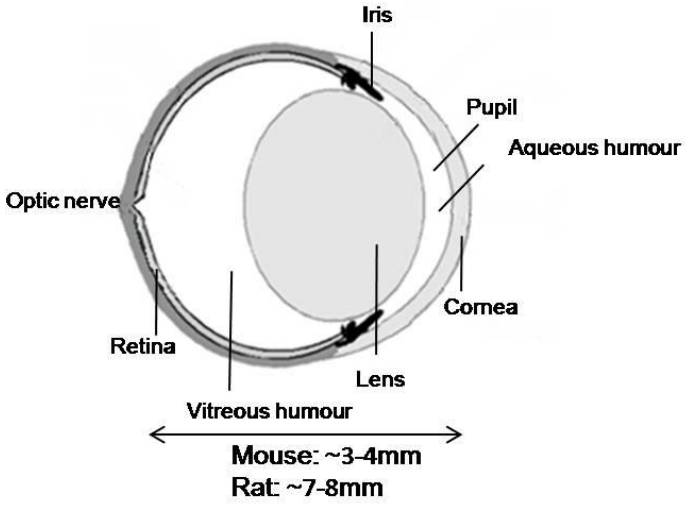

Figure 1-2: Schematic of a mouse or rat eye. (Sketched from histology)

1.3.2 Aberrations in the Rodent Eye

Unlike the human eye, which is designed for high visual acuity, the eyes in mice and rats produce images at the retina which are significantly more blurry [14]. The highly curved surfaces of the small animal eyes introduce significant aberrations into the optical system. In contrast to the refractive power of the human eye, about 60 D, the refractive power of the mouse eye is 500 D [14]. A well known cause of refractive errors comes from highly curved surfaces of the cornea and the crystalline lens. As in humans, the cornea is responsible for most

of the focusing because of the large difference in refractive index between it and the external environment (air) [14]. The small spherical crystalline lens provides less focussing because it is immersed in the vitreous humour which has a similar refractive index, but it is still a source of aberrations.

Imaging through the cornea can be a major concern for detailed visualization of the retina *in vivo* [14]. In order to overcome the aberrations of the cornea, when imaging small animals a flat coverslip lens is used to compress the cornea. This is a standard technique used by other researchers for fundus imaging in small animals. With the refraction at the cornea mostly cancelled out, a converging beam incident on the eye will focus at the retina. The remaining refraction from the crystalline lens can be compensated for by having modest focus adjustment capabilities in the lens system.

1.3.3 Tadpole eye

Xenopus laevis is a species of South African aquatic, which is also been used in visual research in addition to mice and rats. As a research subject, *X. laevis* has advantages over other common laboratory animals as they have a high number of offspring, low maintenance requirements, and a very long

lifespan. However, at present, detailed assessment of *X. laevis* retinal morphology and substructure can only be achieved by histological examination after the animals are euthanized. Because of this, researchers' ability to evaluate the presence or progression of retinal disease in a given animal is limited. In order to identify animals with retinal disease and perform longitudinal studies for monitoring retinal disease progression in individual animals, a non-invasive *in vivo* assessment of the retina without sacrificing the animal is required. A schematic of the *X. laevis* eye is presented in Figure 1-3. The size of the eye is less than 1mm which is much smaller than that of the mouse. Combined with a small pupil, diagnostic imaging of the retina is challenging.

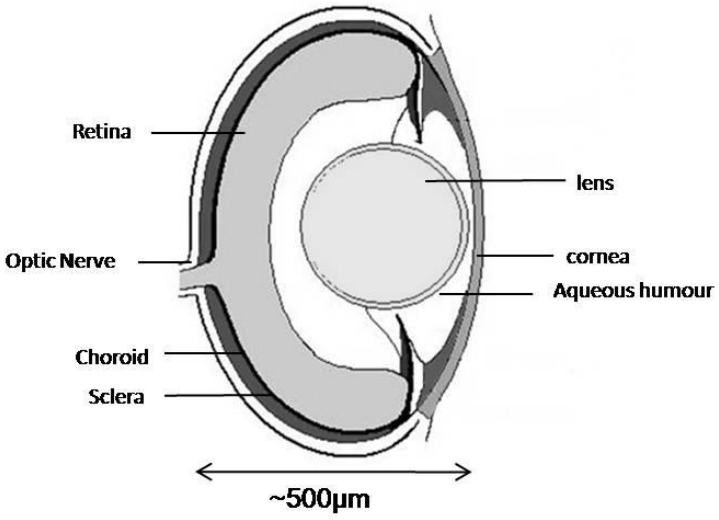

Figure 1-3: Schematic of a *X. Laevis* eye.

1.3.4 Non-Invasive imaging

There is a variety of retinal imaging modalities such as Fundus Photography [7], Scanning Laser Ophthalmoscopy (SLO) [6], and Optical Coherence Tomography (OCT) [1] for human retinal imaging. Fundus photography provides simple, *en-face* images of the retina, showing vasculature and discoloration due to physiologic abnormalities, but does not provide cross sectional information. SLO can be combined with confocal techniques to provide high lateral resolution images of the retinal cells, and depth sectioning on the order of tens to hundreds of microns. So far, the only technique which permits high resolution (micron scale) visualization of the retinal cell layers is OCT.

OCT is a non-contact, non-invasive medical imaging modality for micrometer scale sub-surface imaging of biological tissue over small distances [1][2][3][4]. OCT is similar in principle to ultrasound, but the imaging is performed by measuring light instead of sound. It is greatly used in ophthalmic imaging and it is important as a non-invasive retinal imaging tool to accelerate drug development and gene therapy by basic scientists and medical researchers. Standard resolution OCT provides axial resolutions smaller than 10 μm in the retina which is sufficient to identify the retinal cell layers. The development of

high-resolution optical coherence tomography using broadband light sources has yielded axial resolutions of 2 to 3 μm in the retina [5][9] (more details in Chapter 2).

1.4 Thesis objectives and organization

OCT serves as a practical and indispensible tool for real-time imaging of the microstructures of the retina in vivo and for diagnosing ocular diseases such as age-related macular degeneration, diabetic retinopathy and glaucoma. Nowadays, commercial OCT systems are available for human retinal imaging. However, these systems are highly specific to human imaging, and are not well suited to rodent imaging.

The objective of this thesis is to investigate retinal imaging in small animals with OCT. Human retinal imaging systems cannot be directly used due to the small physical size and poor optical quality of rodent eyes. A prototype SD OCT system and custom sample arm optics was designed to image retinal structures in mice, rats, and *X. laevis*. The utility of the SD OCT system to quantify changes in retinal thickness due to various forms of retinal degenerative diseases was investigated.

The remainder of this thesis concentrates on the prototype SD OCT system and analysis of retina data acquired from small animals. The optical design for SD OCT system for small animals will be introduced in Chapter 2. A validation study comparing OCT imaging with histology for retinal imaging in wild type and transgenic mice with retinal degeneration is presented in Chapter 3. A longitudinal study of retinal degeneration in a rat model of glaucoma using SD OCT is presented in Chapter 4. The results from an investigation into the ability of OCT to image retinal degeneration in *X. laevis* larva are presented in Chapter 5. This thesis concludes with a discussion of future work.

2. SD OCT SYSTEM DESIGN FOR SMALL ANIMAL

In this thesis, Fourier Domain (FD) OCT is investigated as a non-invasive tool for retinal imaging in small animals. The research focus in OCT has shifted from traditional time domain to so-called Fourier Domain detection because the spectrally resolved detection leads to additional sensitivity improvements over the classical time domain systems [6]. FD OCT systems have two configurations: Spectral Domain (SD) OCT and Swept Source (SS) OCT. SD OCT uses a grating to spatially disperse the spectrum across an array-type detector, and in SS OCT a narrow band laser is swept across a broad spectrum, encoding the spectrum as a function of time. In this thesis, only SD OCT will be described in detail, but the overall processing is identical for SS OCT.

2.1 Spectral Domain Optical Coherence Tomography

A simplified optical setup of SD OCT system using a Michelson interferometer-type configuration is illustrated in Figure 2-1.

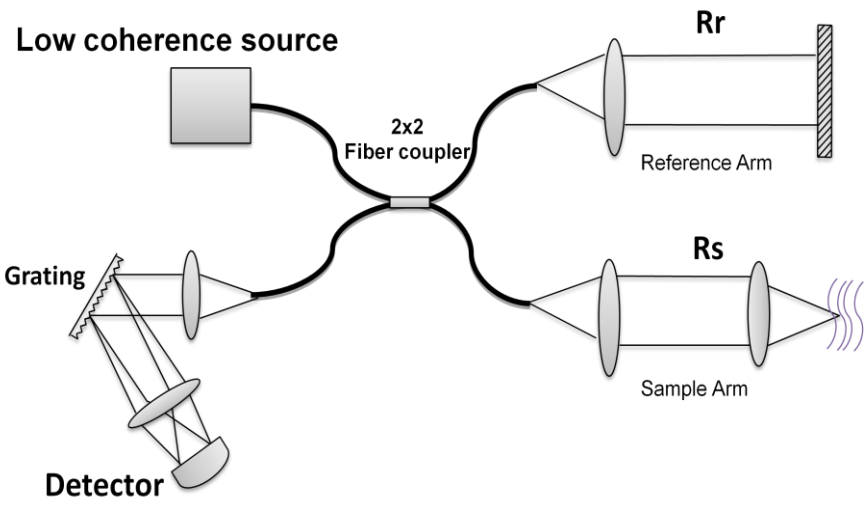

Figure 2-1: Standard Michelson-type interferometer setup used in OCT

Light from a low coherence source is divided by a 2x2 fiber coupler into two paths. The back reflected light from the sample and stationary reference arms, R_S and R_R recombine in the fiber coupler and interfere to produce fringes corresponding to the optical path length mismatch between the two paths, Δz. The spectrometer permits the interference fringes to be measured as a function of wavelength. The equation for the spectral interferogram acquired at the detector is written as,

$$\mathbf{I_D(k) = S(k)[R_S + R_r] + S(k)\left[2\sqrt{R_S R_R}\cos(2\Delta zk)\right],} \qquad \textbf{Eq 2-1}$$

where S(k) represents the source spectrum in units of wavenumber, with units of inverse distance. In SD OCT, the optical path length difference is encoded by the

frequency of the interferometric fringes as a function of the low coherence light source spectrum.

The Fourier transform is used to extract the frequency content of the acquired signal. The Fourier transform pair of distance is wavenumber k. To obtain the location of each reflector, we take Fourier transform of Eq 2-1 generating,

$$\hat{\mathbf{I}}_{\mathbf{D}}(\mathbf{z}) = \hat{\mathbf{S}}(\mathbf{z})[\mathbf{R}_{\mathbf{S}} + \mathbf{R}_{\mathbf{r}}]\boldsymbol{\delta}(\mathbf{z}) + \hat{\mathbf{S}}(\mathbf{z})\mathbf{2}\sqrt{\mathbf{R}_{\mathbf{S}}\mathbf{R}_{\mathbf{R}}}[\boldsymbol{\delta}(\mathbf{z} - \mathbf{2}\Delta\mathbf{z}) + \boldsymbol{\delta}(\mathbf{z} + \mathbf{2}\Delta\mathbf{z})], \qquad \textbf{Eq 2-2}$$

where $\hat{S}(x)$ is the Fourier transform of the source spectrum. $\hat{S}(x)$ represents the axial resolution of the OCT system, and is inversely related to the source bandwidth by the Fourier transform. $\hat{S}(x)$ is convolved with two terms in Eq 2-2: the first term is the DC term at zero path length mismatch due to the non-interfering components of the reference arm, and the second term represents the location of the reflector and its complex conjugate image. The complex conjugate peak arises because the detector does not measure the phase of the interferogram, which is required to uniquely determine the location of the scatterer. This symmetry, referred to as the complex conjugate artifact, reduces by half the usable depth range in SD OCT (i.e. only positive or negative distance). A schematic example of OCT acquisition is presented in Figure 2-2. The Fourier

transformed signal in Eq 2-2 is called an Axial Scan (A-scan) and represents the depth information at a single point on the surface sample. In order to obtain a two dimensional cross sectional slice through the image, the position of the OCT beam must be scanned across the sample.

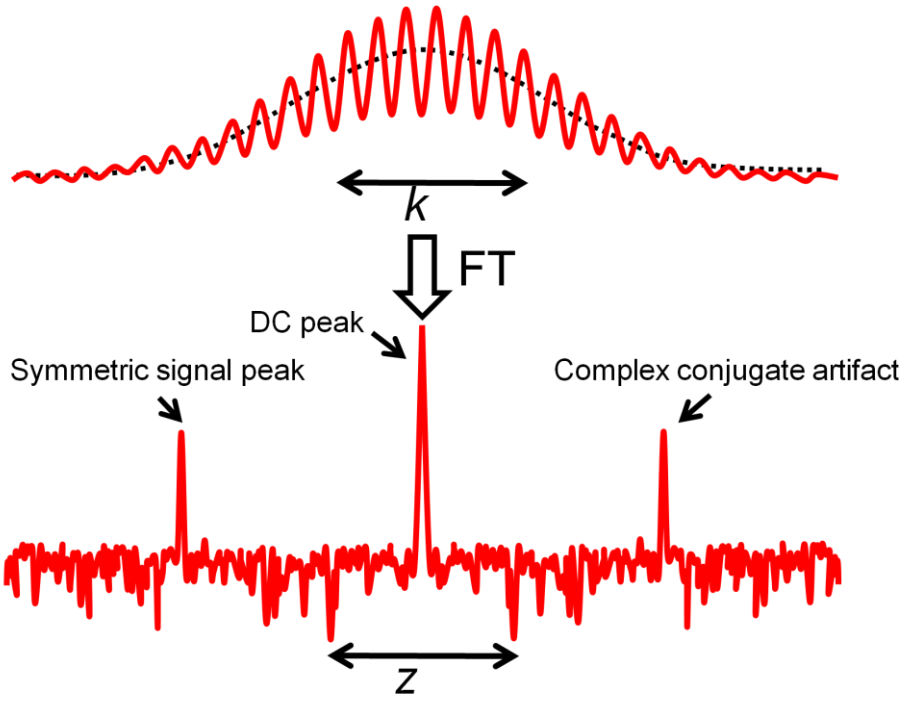

Figure 2-2: The Fourier transform of an OCT interferogram results in three peaks, one at DC and two symmetric peaks.

2.2 Topology of Interferometer and Spectrometer

The SD OCT system used in this study utilized a cost-effective and portable continuous Super Luminescent Diode (SLD) light source (Superlum Diodes, Ltd, Moscow, Russia). The SLD source has a central wavelength of 826nm and a spectral bandwidth full width half maximum (FWHM) of 72nm. The

source spectrum from test results made by Superlum is reproduced in Figure 2-3. The axial resolution for a Gaussian spectrum centered at 826nm with FWHM of 72nm is 4μm.

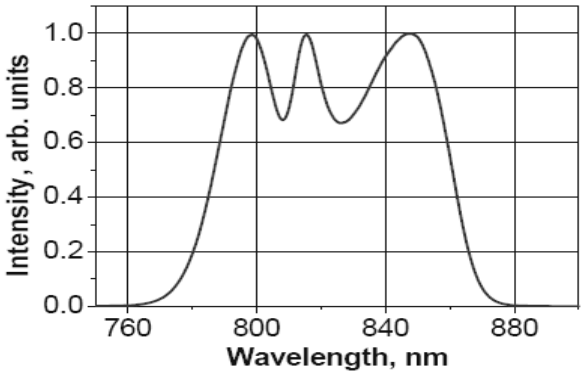

Figure 2-3: The spectrum of the SLD source.

The OCT interferometer was constructed from a 2x2 fiber coupler with a 70/30 splitting ratio. Light was divided by the fiber coupler into two paths which provides 70% of the light to the reference arm and 30% to the sample arm. The reason for this configuration is that on the backward path, 70% of the light collected from tissue in the sample arm is directed to the detector to optimize the optical signal. Two fiber couplers were used in our system to give control of the power in the sample and reference arms, and reduce the amount of backreflected or backscattered light from both arms returning to the SLD, as shown in Figure 2-4.

The reference arm simply consists of a collimating lens, an reflective attenuator (metallic neutral density filter), and a mirror. The reason of using an attenuator is to lower the power of back reflected light from the reference arm in order to avoid saturating the detector and damaging the SLD.

The sample arm in the system, shown in Figure 2-5, consists of a collimating lens followed by a pair of galvanometric mounted mirrors (galvos) (Cambridge Technology) for raster scanning control of the beam, a beam expander and an objective lens. In order to generate a B-scan, the beam position is scanned across the sample using the galvos which provide lateral X-Y raster scanning by using two mirrors with a 3mm clear aperture. The galvos have 40 mechanical degrees of angular freedom. The command waveform was generated using a National Instruments Data Acquisition Multi-Function (NI-DAQmx) computer peripheral and output to the galvos to control X and Y position. The beam expander was placed after the galvos to provide a flexible design of different depth of focuses for imaging different types of tissue. The position of the second lens of the beam expander was made adjustable in order to give the beam freedom to focus on different depths in the sample. An objective lens was used after the beam expander to focus the light onto the sample. The details of

the sample arm lenses are specific to the subject being imaging, and are discussed in next section.

The high speed spectrometer used was a custom design constructed using 1200 line/mm transmission diffraction grating. The detector was a 1024 element high speed Gigabit Ethernet (GigE) camera from Dalsa (Waterloo, Canada), with 14 μm square pixels. The camera could operate at a maximum line rate of 68kHz, but was typically reduced to 20kHz for imaging. The interfered light comes out from the fiber and gets collimated by a convex lens. The collimated beam projects on the grating which separates all wavelengths. After the grating, the entire beam representing different wavelengths travel through a combination of convex lenses to get focused on the detector. The overall setup is shown in Figure 2-4.

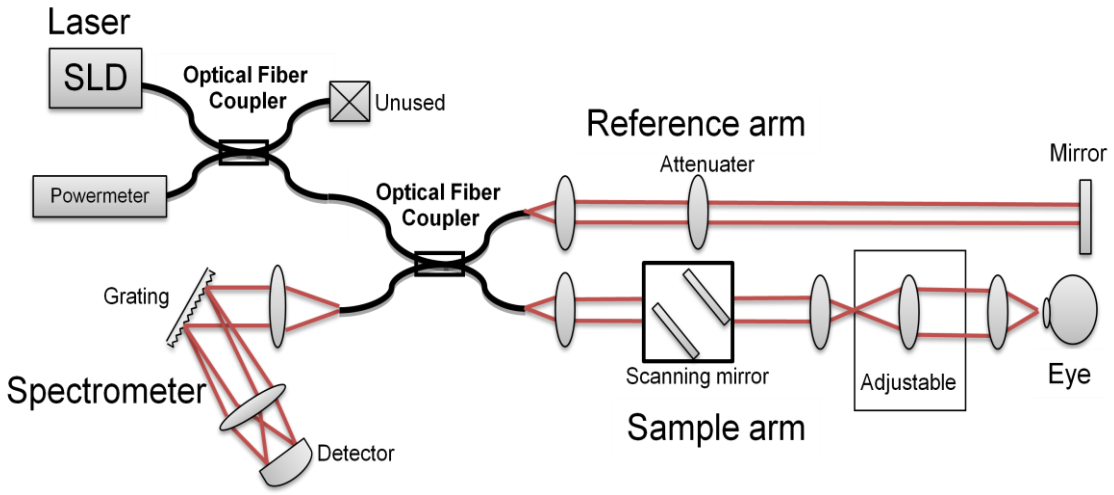

Figure 2-4: Overall setup for current SD OCT system for small animal imaging.

2.2.1 Sample arm design for retinal imaging in small animals

As discussed in Chapter 1, the highly curved cornea in small animal eyes can be a severe source of optical aberrations. For retinal imaging in rats and mice, a cover slip was placed against the front of the eye to cancel out the refraction of the cornea. The refraction caused by the crystalline lens inside the small animal's eye was ignored.

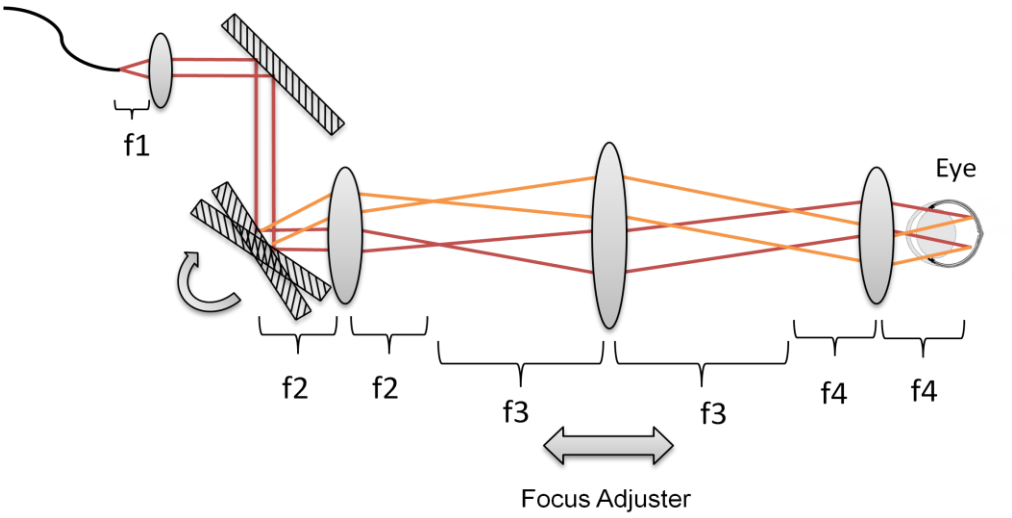

Figure 2-5: Sample arm optical system setup. The labels f1, f2, f3 and f4 are the focal lengths of each of the lenses. The light enters and exits the sample arm optical fiber.

The four-lens systems for each type of experimental subject were designed by choosing the best stock lenses to match the depth of focus with the thickness of the animal retina using Gaussian optics calculations. For the mouse retina the lens combination used was: a 4.5mm collimator, a 2x beam expander using 25mm and 50mm lenses, and a converging 25mm (objective) lens. This lens combination provided a calculated 278μm depth of focus, which is slightly longer than the average thickness of a mouse retina which is around 230μm. The reason of using the 4.5mm convex lens for the first one is to make a collimated beam which will fit on the galvos (maximum beam diameter of 3mm). The focal length of the third lens was changed to vary the depth of focus for

different samples, as listed in Table 2-1. Achromatic lens doublets where used for the majority of the lenses, except for the collimating lens where we used an asphere because short focal length achromats were not available.

Table 2-1 Design parameters for different sample arm optics

Parameter	*Mouse*	*Rat*	*Tadpole*
NA	0.12	0.12	0.12
λ (μm)	0.83	0.83	0.83
f1 (mm)	4.5	4.5	4.5
f2 (mm)	25	25	25
f3 (mm)	50	45	100
f4 (mm)	25	25	25
Depth of Focus (μm)	278	343	70

2.3 Slit Lamp Integration

There were three sample arm setup iterations. The initial setup was mounted on a linear translation stage. This only allowed one inch translation in each of the X, Y, and Z directions as shown in Figure 2-6. Although this setup could be used for imaging, it was challenging to align to the correct location on the mouse eye. A more sophisticated setup was required with more degrees of freedom.

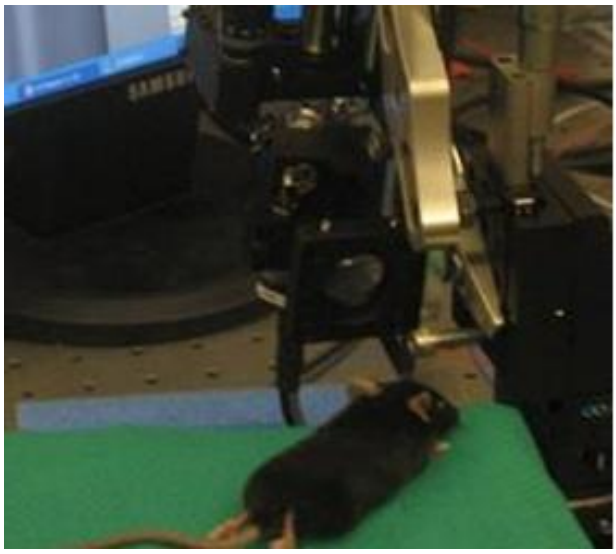

Figure 2-6: The hand-held scanner shown attached to a 4 degree of freedom stage. The mouse shown was anesthetized for imaging.

In the second generation of the sample arm, an aluminum plate was designed to integrate the OCT sample arm optics in a compact fashion, and mounted them on a standard slit lamp biomicroscope to facilitate alignment to the samples. The joystick allowed free movements by shifting forward, backward, laterally or diagonally. Rotation of the joystick lowered or elevated the beam position. The final optical plate design, shown in Figure 2-7, was designed in Solidworks by Mei Young and machined at the Simon Fraser University (SFU) Science Machine shop. It was an improvement on the previous design by including a linear stage adjustment for the focusing lens.

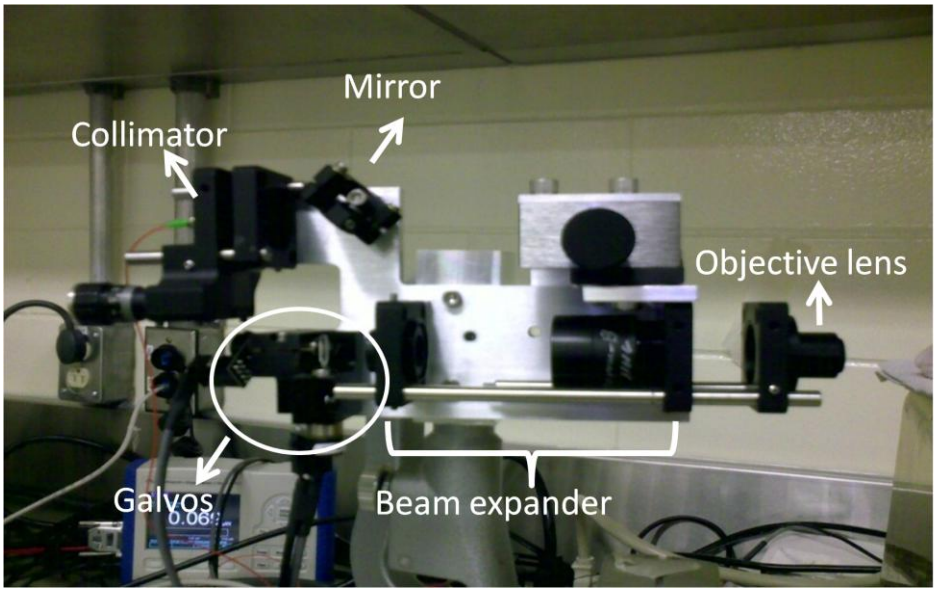

Figure 2-7: Optical plate design on slit lamp biomicroscope.

During imaging, the subject (e.g. rat) was placed comfortably on a stage with the eye to be examined facing the beam as shown in Figure 2-8.

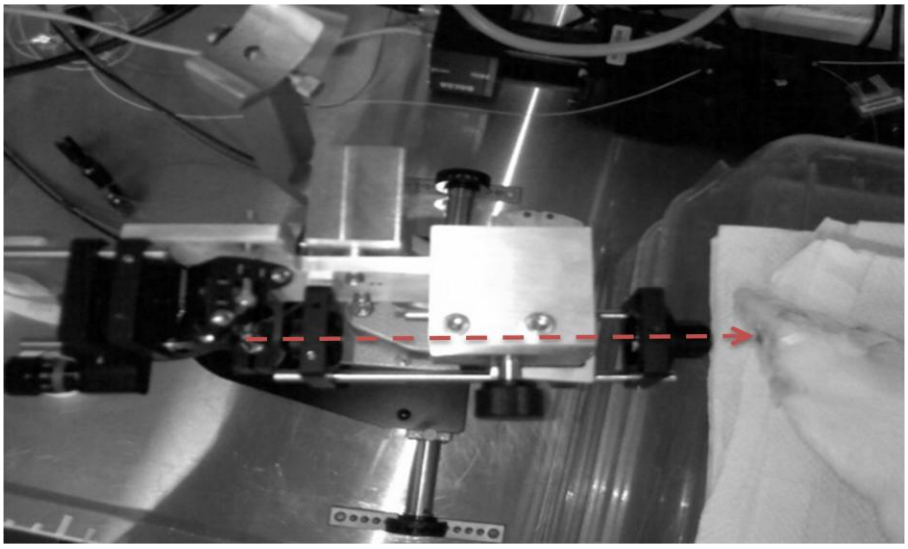

Figure 2-8: A rat eye was positioned to be imaged. The red dashed line represents the beam path.

The slit-lamp mounted system was used for validation studies in the subsequent chapters.

2.4 Imaging procedure

Real-time data acquisition was performed using a custom software package developed in Biomedical Optics Research Group (BORG) at SFU called the OCTViewer shown in Figure 2-9, written in C++ for rapid frame grabbing, processing, and display of two dimensional images.

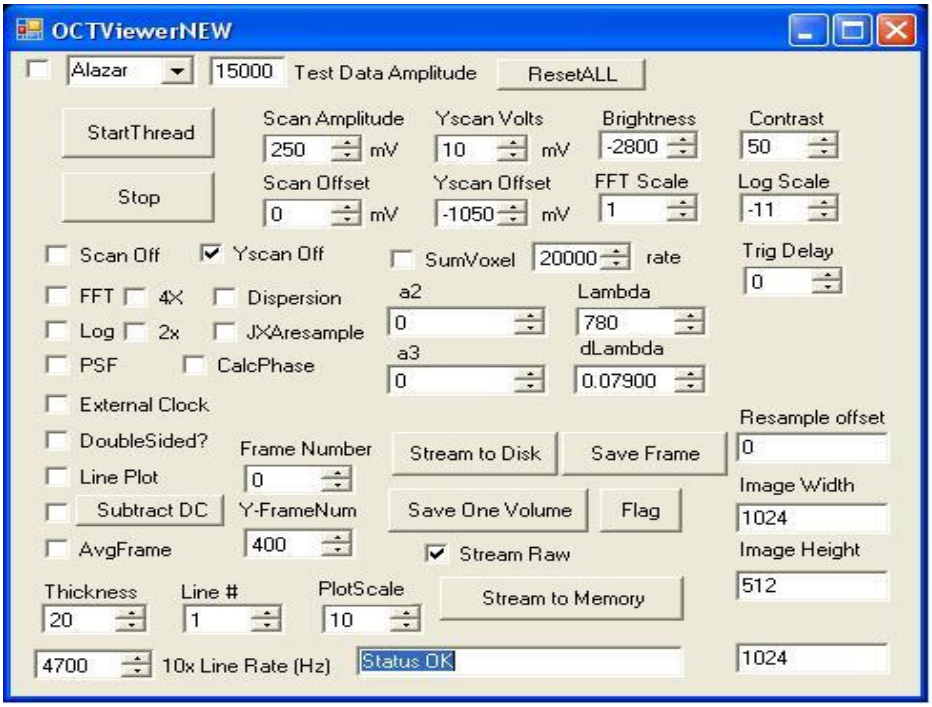

Figure 2-9: OCTViewer interface.

Before acquiring data, there are some parameters that need to be prepared. The displayed image width (number of pixels in the linescan camera)

and height (number of A-scans in a frame) can be set by user through the interface of the OCTViewer software. For normal acquisition with the Dalsa camera, the image width was set to 1024 and image height to 512. The Scan Amplitude controlled the signal to the galvos, and accordingly the physical scan length. The number of frames can be user selected to determine the number of elevations in the data volume acquired by raster scanning the beam using both galvo mirrors. The scanning sequence on a volumetric dataset is shown in Figure 2-10. In the figure, the fast scan axis is in the X-direction, and the slow scan axis (adjacent frames) is in the Y-direction.

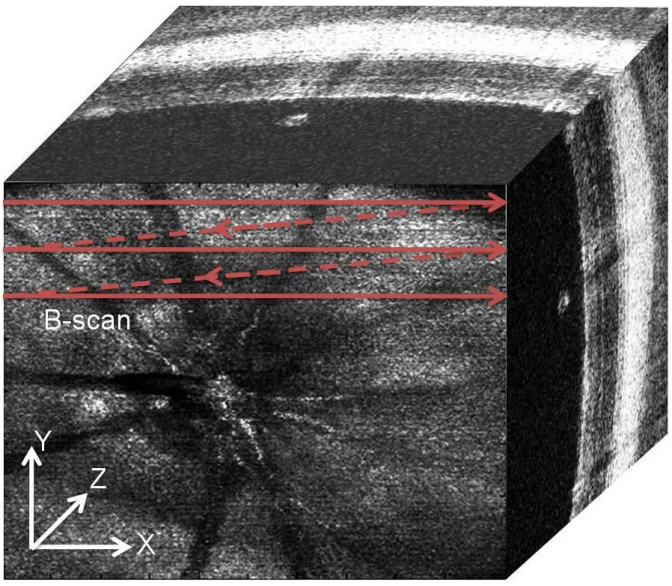

Figure 2-10: Scanning sequence of the galvo in volumetric image acquisition. X: image width. Y: images height. Z: image depth of system. The red solid line is each single B-scan (X scan).

The fringe data was processed into image data using OCTViewer. Processing was performed in real-time and included DC subtraction of the reference arm spectrum, re-sampling of the interferometric data from linearly sampled in wavelength space to linear sampling in wavenumber space, fast Fourier transform (FFT), and contrast and brightness. Re-sampling is required because the natural pairing of the Fourier transform is space to wavenumber. However, the spectrometer samples the interferogram linearly in wavelength, which is inversely related to wavenumber, meaning that the samples of the interferogram are not evenly spaced in wavenumber. Failure to re-sample the interferogram to be linearly spaced in wavenumber results in a distorted image.

Another source of distortion in OCT imaging is dispersions. Dispersion is the term used to describe the effect that optical materials have a different optical path length for the range of wavelengths used in the low coherence source. In retinal imaging, the sample beam propagates through the cornea, aqueous, lens, and vitreous of the eye before it reaches the retina. Significant dispersion occurs from propagation through the vitreous and lens, which comprises the majority of the eye length [18]. Dispersion compensation can be performed numerically by adding a phase term to the interferogram before performing the Fourier transform.

This is required to match the path length difference of the two interferometer arms over the bandwidth of the light source in order to achieve high image resolution. Different subjects have different eye lengths; therefore, dispersion compensation needs to be adjusted for individual subjects. The flow chart for dispersion compensation is shown below in Figure 2-11 [16]. The algorithm was refined and adapted for integration into the OCTViewer code. A high speed library provided by Intel called Intel Processing Primitives (IPP) was used to streamline calculations.

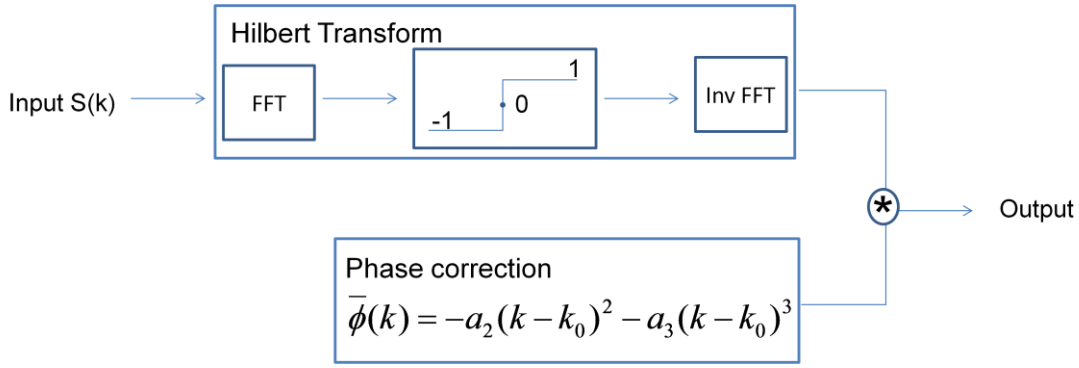

Figure 2-11: Flow chart of SD OCT dispersion compensation procedure. The Hilbert transform is used to calculate the complex representation of the input signal. The phase of this signal is modified by using adjustable second- and third-order terms.

The effects of re-sampling and dispersion compensation on the image quality are profound. By manually adjusting the second-order and third-order dispersion terms, we could get significant improvement in the image resolution.

An example is shown below in Figure 2-12. The different shades of gray in Figure 2-12 (b) correspond to the backscattering intensity from different retinal layers.

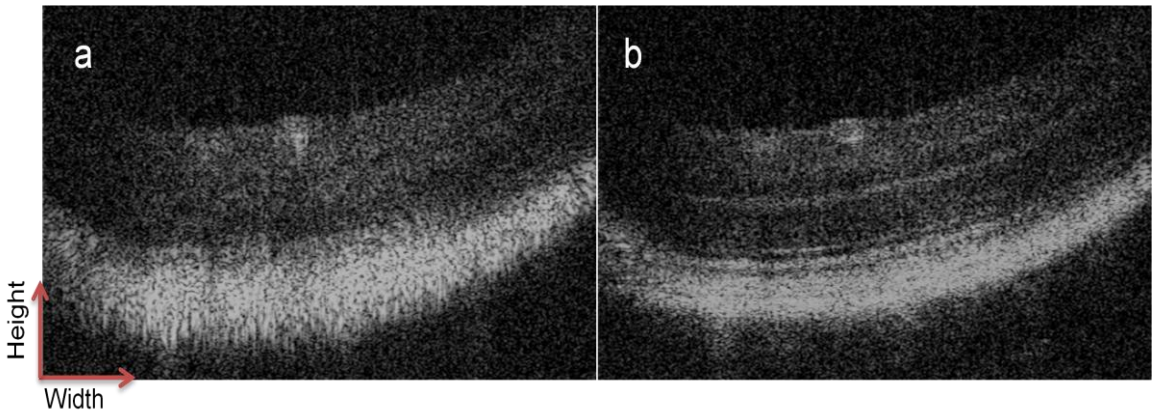

Figure 2-12: (a) A mouse retina image without re-sampling and dispersion compensation, (b) the image with re-sampling and dispersion compensation. The retinal layers are significantly better defined in the dispersion compensated image. (Width: 2.5mm, Height: 350μm)

2.5 Fundus imaging with OCT

The *en face* fundus image, shown in Figure 2-13 (a) was constructed by summing the values of each A-scan, mimicking the operation of an SLO [19]. The strength of the OCT imaging modality is that depth information is acquired at each point on the fundus image. The optic nerve head (ONH) cross sectional image presented in Figure 2-13, was extracted from the position in the fundus image represented by the red solid line in Figure 2-13 (b). The B-scan was enhanced using simple Gaussian spatial filtering to smooth out the speckle.

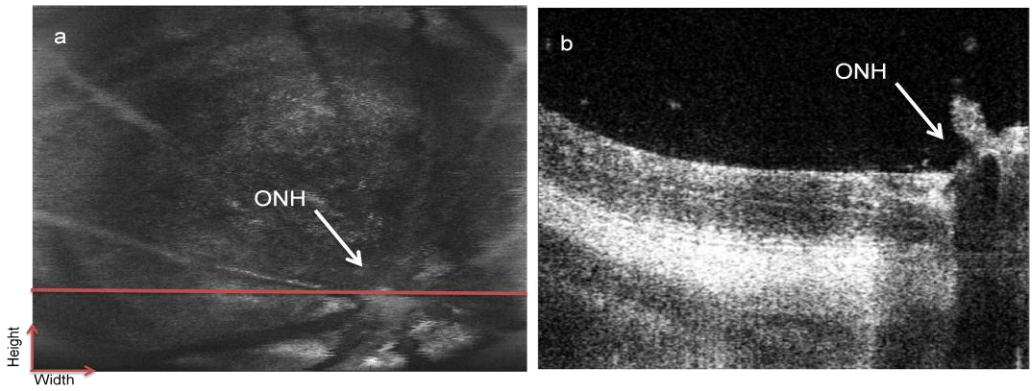

Figure 2-13: (a) *En face* fundus image of a rat eye with ONH in the middle (b) a cross sectional image extracted from the position of the red line. (Width: 4mm, Height: (a) 4mm (b) 800µm)

A software package called Amira was used to reconstruct volumetric images of the data set. Amira facilitates visualization of the cross sectional planes and *en face* profiles as presented in Figure 2-14.

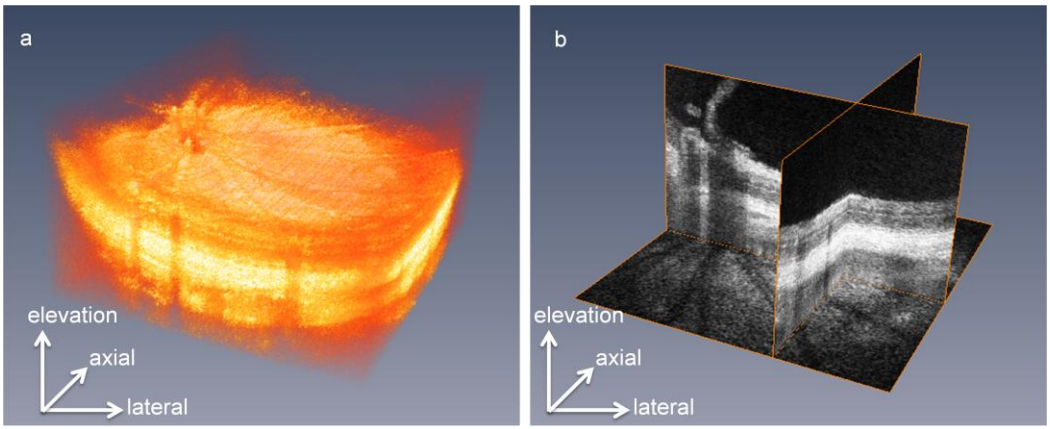

Figure 2-14: (a) Volumetric image of the rat retina generated using Amira software. (b) Image planes in all three dimensions. (axial: 600µm, elevation: 4mm, lateral: 4mm)

In the next chapter, the preliminary research comparing OCT imaging in mice to histology was performed using this SD OCT system.

3. THE VALIDATION OF SD OCT IN THE MOUSE MODEL OF X-LINKED JUVENILE RETINOSCHISIS

Investigation of retinal degeneration with SD OCT in rodents is at an early stage, and previous to this study only wild type (WT) specimen and simple models of retinal degeneration have been imaged [20][21][22]. In this SD OCT research application, the mouse model for X-linked Juvenile Retinoschisis (RS), a form of genetic retinal degeneration in males, was investigated. These transgenic mice are deficient in the Rs1h gene, and have been shown through histology to be characterized by holes in the Inner Nuclear Layer (INL) [16], disorganization of the retinal cell layers, and slow progressive degeneration of the photoreceptors. The objective of this study was to compare non-invasive retinal imaging in *Rs1h* knockout (KO) and wild type mice acquired with the SD OCT to invasive histological sections. Qualitatively, disorganization of the retinal layers associated with *Rs1h* knockout mouse was observed with SD OCT, as well as holes in the INL which is characteristic of retinoschisis.

The application of SD OCT to provide quantitative measurements was also investigated. The metric used to quantify the amount of retinal degeneration was the thickness of the Outer Nuclear Layer (ONL) which thins significantly with increasing age in *Rs1h* mice. The amount of retinal degeneration in *Rs1h* mice was compared to age match wild type mice by measuring the thickness of the ONL. Two dimensional maps of the ONL thickness were extracted from the SD OCT volume data acquired on wild type and *Rs1h* knockout mice to demonstrate the potential power of SD OCT to measure ONL thinning across the surface of the retinal.

3.1 Methods

A prototype SD OCT system was constructed for mouse retinal imaging. The setup used in this application, previously presented in Figure 2-4, consisted of the sample arm design providing a 278μm depth of focus. The corresponding transform limited axial resolution was nominally 4 μm in tissue, calculated from the SLD source bandwidth. During animal imaging, the optical power output from the source was reduced to 770μW, the American National Standard for Safe Use

of Lasers (ANSI) limit for maximum exposure of the retina to continuous light at this wavelength [23].

Images of the retinas from wild type and *Rs1h* knockout mice were acquired non-invasively using SD OCT with the specimen anesthetized. At the completion of the non-invasive SD OCT imaging, invasive retinal cross sectional images (histology) were acquired from a nearby region for comparison to the SD OCT images.

3.1.1 SD OCT mouse imaging

Although the SD OCT imaging is non-invasive, in order to keep the mice still during imaging, they were anesthetized using an intraperitoneal injection of ketamine and xylazine mixture (0.1ml per 10 g body weight). After anesthetization, the mouse was placed gently on a heating pad to maintain warmth, and simple manual manipulation was used to rest the head of the mouse in an orientation where the angle of the eye was properly coupled to the optical beam. The pupils were dilated using a topical solution (atropine sulphate 1%). Refraction of light at the cornea was cancelled by placing a flat coverslip generously coated with a generic artificial tear gel over the eye. Alignment of the

optical system to the mouse retina required several minutes, and was followed by rapid acquisition of data, requiring nominally 10 seconds per volume. During imaging, the software displayed the SD OCT B-scans at ~30 frames per second. Registration of the location of the B-scan within the two dimensional surface of the retina was performed by switching the display mode to a higher speed (60kHz line rate), low sampling density area scan, representing a reconstructed fundus type image. All mouse handling adhered to the ARVO Statement for the Use of Animals in Ophthalmic and Vision Research, and were performed under protocols compliant to the Canadian Council on Animal Care with the approval of the University Animal Care Committee at SFU.

The ONL thickness measurements were extracted by post processing saved data. A fundus type image of the mouse retina was reconstructed using the SD OCT volumetric data, and used to register the location of the ONL thickness measurement 400 micrometers from the optic nerve head where the retinal layers were of nominally constant cross section. The ONL boundaries were delineated by manually placing points at the boundary between layers, and fitting a low order polynomial to the points using mathematical software package MatLab (MathWorks, Natick, MA, USA). The ONL thickness was subsequently

measured along a line in the image, and was calculated perpendicular to the curvature of the retina using Snell's law calculations to account for refractive index changes [24][25]. The estimated average refractive index of the retina was n_{retina} = 1.38. The recorded ONL thickness for a given eye was calculated as the mean of three adjacent depth profile frames to average out human error in delineation of the ONL boundaries. Following the non-invasive SD OCT measurement, the mice were euthanized and the eyes were enucleated for histology.

3.1.2 Histology

Histology was performed immediately following SD OCT measurements by Dr. Laurie Molday (UBC). After fixation, the samples were washed and frozen in O.C.T. compound, cut into 12μm sections and stained with DAPI nuclear stain. The retina sections were visualized with under a Zeiss Axioplan fluorescence microscope and the ONL thickness was measured by counting the number of nuclei at five locations in the DAPI stained histological sections.

3.2 Results &Discussion

3.2.1 Correlation of SD OCT depth profiles with histological sections

Cross sectional depth profiles in SD OCT consist of alternating bright and dark regions, corresponding to the backscattering intensity of the various retinal layers. The retinal layers can be identified in the SD OCT images through comparison with a histological section as shown in Figure 3-1(a, b). The thickness of the ONL was measured as the distance of the dark band between the bright lines constituting the outer plexiform layer (OPL) and the inner segment (IS) of the photoreceptor layer. In order to measure the thickness of the ONL, each SD OCT image was first manually segmented by selecting points on each curved boundary and fitting them to a low order polynomial, as described in the Methods section. In Figure 3-1(b), the OPL/ONL boundary is indicated by the green line fit to the manually selected points represented by the circles. The ONL/IS boundary was similarly delineated, and is represented in yellow.

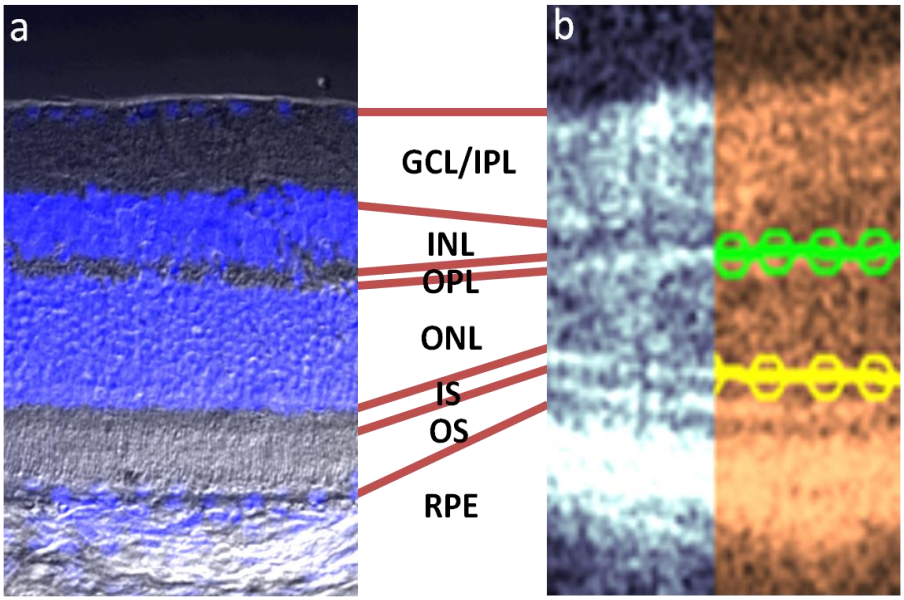

Figure 3-1: Comparison of the wild type mouse retinal layers observed in (a) DAPI stained histological section merged with DIC to (b) non-invasive SD OCT. The retinal layers were segmented manually and a fit to a fourth order polynomial which was subsequently used for the thickness measurement. GCL, ganglion cell layer; IPL, inner plexiform layer; OPL, outer plexiform layer, ONL, outer nuclear layer; IS, inner segment; OS, outer segment. This figure was reproduced from [26], and is copyrighted by the Association for Research in Vision and Ophthalmology.

3.2.2 ONL Thickness Measurements with SD OCT and histology

For this study, the measurements of the ONL thickness were compared in *Rs1h* knockout (KO) mice to that of their wild type counterparts. The ONL thickness was measured in both eyes of each specimen used. The control group consisted of 6 wild type mice for the SD OCT measurement, corresponding to a sample size of n = 12 eyes. The control group for the DAPI stained histology (performed at UBC) consisted of five specimens, corresponding to a sample size

of n=10 eyes. Two mice were used for each age group of *Rs1h* KO investigated, making a sample size of $n_{RS1hXmo}$=4 eyes (X represents the age of the specimen in months). Three different ages of *Rs1h* KO mice were used in this study: two months, ten months, and fifteen months. The reported values of ONL thickness represent the average and standard deviation of the n measurements from each group.

Examples of the fundus reconstruction and depth profile images acquired by the SD OCT are presented alongside DAPI stained histology in Figure 3-3. The fundus image represents a volumetric data set; a SD OCT depth scan of information is contained in each horizontal line. Comparison of the *Rs1h* knockout mouse retina images to the wild type counterparts indicates a visible difference in the retinal layer structure. Most noticeably, the OPL and IS/OS layers were not well defined in the SD OCT images of the *Rs1h* knockout mouse retina, and appeared as broader regions of high scattering intensity. This is consistent with earlier reports using histology where the disruption of the cell layer architecture was notable in the OPL between the ONL and INL [25].

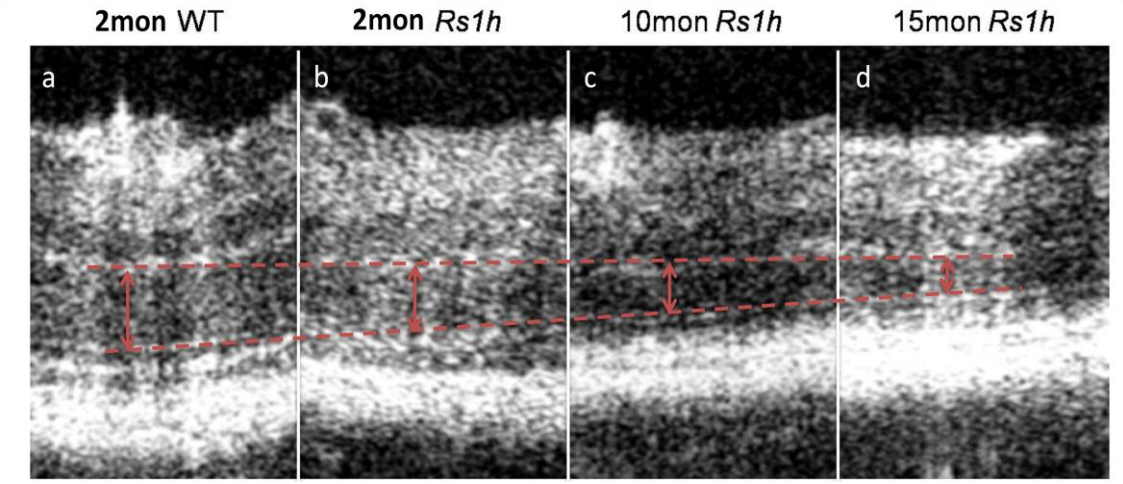

Figure 3-2: Representative sections of B-scan images for 2 month, 10 month and 15 month group. (a) A control ONL thickness from wildtype mouse. (b – d) The red dash lines indicate the progressive loss of ONL thickness over time.

The numerical results of the ONL thickness measurements comparing SD OCT to DAPI stained histology are summarized in Table 3-1. The ratio was calculated using the average ONL thickness measurement from each *Rs1h* KO group and dividing it by that of the corresponding control group. Standard error propagation was used based on the standard deviation of the group averages. The measured differences in ONL thickness between *Rs1h* KO mice of neighbouring age groups in the time course study was statistically significant ($p<0.01$, by ANOVA).

Table 3-1 ONL thickness measurements from *Rs1h* KO mice using SD OCT and DAPI stained histology. The ratio was calculated using the ONL thickness of the control group. Nuc., Number of nuclei counted from histology.

	Measured Thickness				**Ratio**			
	OCT		Histology		*Rs1h*/WT			
month	μm	SD	Nuc.	SD	OCT	SD	Nuc.	SD
2	31.8	0.7	7.6	0.4	0.69	0.03	0.67	0.07
10	27.2	0.4	6.4	0.6	0.59	0.03	0.56	0.07
15	17.0	0.5	3.1	0.5	0.37	0.02	0.28	0.05

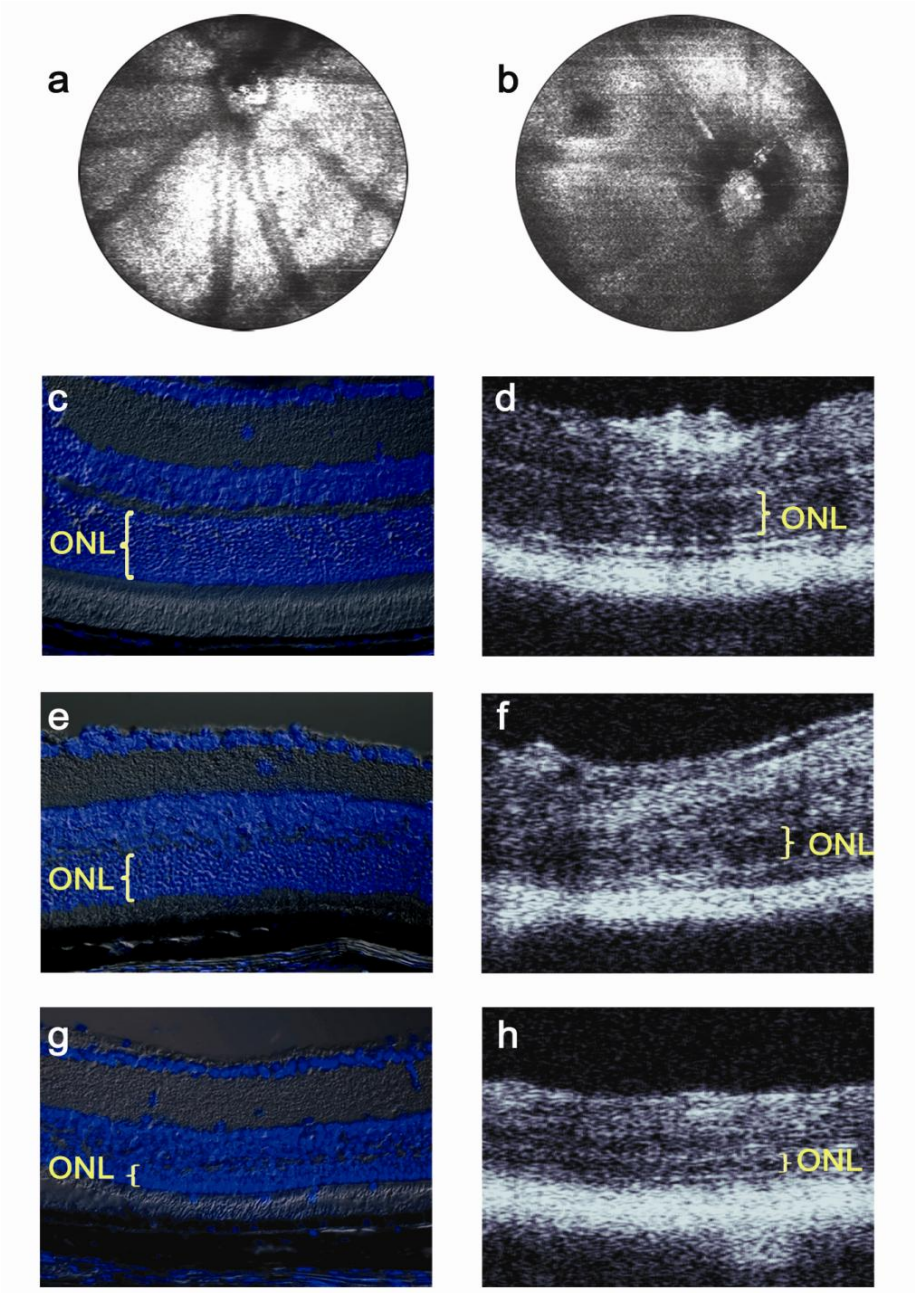

Figure 3-3: Fundus-type images reconstructed from SD OCT data acquired from (a) WT and (b) *Rs1h* KO mice. DAPI stained histology and SD-OCT images from the same mice are shown for (c, d) 2 month old WT, (e, f) 2 month old *Rs1h* KO, (g, h) 15 month old *Rs1h* KO. This figure was reproduced from [26], and is copyrighted by the Association for Research in Vision and Ophthalmology.

3.2.3 Discussion

Non-invasive imaging of the mouse retina can be a powerful tool for characterization of retinal degeneration. Imaging mice with the SD OCT system poses a different set of challenges than human retinal imaging. The SD OCT configuration for imaging humans typically uses a collimated beam of light incident on the eye, relying on the refractive elements of the cornea and lens to focus the beam on the retina. In this investigation, it was preferable to cancel out the refraction at the cornea with a contact lens and perform SD OCT imaging of the mouse eye using a converging beam [42].

In the SD OCT images, irregularities in the retinal layer structure of the *Rs1h* knockout mouse were observed relative to the wild type. A sample SD OCT image of an *Rs1h* KO mouse is shown adjacent to a histological section in Figure 3-4 (a, b). The OPL layer and the IS/OS photoreceptor layers appear thicker in the SD OCT image due to poorly defined ONL boundaries. In the DAPI stained histological image, the OPL between the ONL and INL is not well resolved. In the SD OCT images, superficial holes in the INL layer were observed in Figure 3-4 (b) as dark regions with no backscattered light signal.

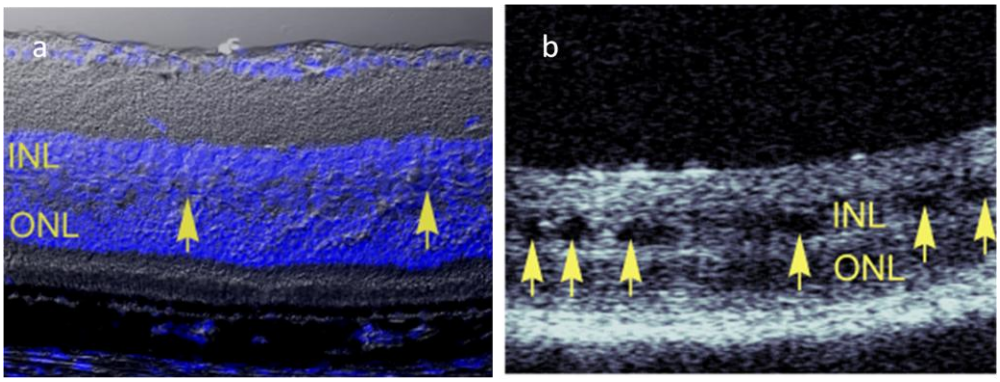

Figure 3-4 Arrows point to holes observed in the inner nuclear layer (INL) of (a)DAPI stained histology and (b) SD OCT image of the retina of a two month old *Rs1h* knockout mouse. This figure was reproduced from [26], and is copyrighted by the Association for Research in Vision and Ophthalmology.

Since shadows of lower scattering intensity were not cast below the holes in the INL, the gaps could be concluded as a full of clear non-scattering fluid. Similar results of holes in the INL had been previously observed in histological samples of this strain of mice [25], but due to the physical manipulation of the retinal samples in histological preparation, it was not clear if the gaps were due to delamination of the cell-to-cell contacts in the INL or if the holes were present in the normal physiology. Due to the non-invasive nature of SD OCT imaging, the retinal holes in the ONL were not conclusively confirmed as the artifacts of histology. The holes observed in the SD OCT images of the *Rs1h* knockout mouse can also be compared with the observation of schisis cavities in the SD OCT images of humans with X-linked Juvenile Retinoschisis [28][29][30]. These

images demonstrate that SD OCT has the potential to be used to non-invasively monitor the size and number of the retinal holes, and provide feedback on the progress of retinal therapy without destroying the specimen.

Quantitative measurements of retinal degeneration were extracted from the data presented in Figure 3-3 to monitor the relative thickness of the ONL in the *Rs1h* knockout mice relative to wild type mice. The averaged ONL thickness measurement of the *Rs1h* KO mice obtained with the SD OCT and with histology is summarized in Table 3-1. The average thickness of the ONL in wild type mice (independent of age) measured with SD OCT was μ_{WT} = 46μm, SD= 2μm (*n* = 12). The standard deviation is less than the axial resolution of the system (~4μm in tissue) and indicates a reasonable correlation of thickness measurements across all of the animals and in both eyes. The average ONL thickness measurement in wild type mice obtained by counting nuclei in the DAPI stained histology was μ_{WT} =11.4 nuclei, SD = 1 nuclei (*n = 10*), indicating an uncertainty of 9% in the wild type mice.

The amount of retinal degeneration in the *RS1h* knockout mice relative to their wild type counterparts is also summarized in Table 3-1. For two month old

mice, the SD OCT measurements indicated that the ONL in *Rs1h* knockout mice had degenerated to μ=69%, SD 3% (*n=4*) of the wild type ONL thickness. This measurement was statistically within experimental error of the same measurement made through histology. Further degeneration of the ONL was observed in the 10 month old *Rs1h* KO mice; with the SD OCT, the measured ratio ONL_{RS1h}/ONL_{WT} was μ=59%, SD 3% (*n=4*). This measurement also agreed with the DAPI stained histology measurements within experimental error. The measured ratio of ONL thickness in the 15 month old *Rs1h* KO mice relative to the wild type was μ=36%, SD 2% (*n=4*). However, due to the advanced degeneration of the ONL and severe disorganization of the retinal layers observed in Figure 3-3 (g, h), delineation of the ONL thickness by SD OCT or DAPI stained histology was nontrivial.

The thickness of the ONL in *Rs1h* KO mice was measured for two additional age groups, five months and fourteen months. The histology measurements for these mice followed the trend observed in the other groups. The SD OCT measurements were used to graph the change in ONL thickness across the age groups; the data is presented in Figure 3-5 (a). The graph suggests that the retinal degeneration in *Rs1h* KO mice is gradual between the

ages of two months and nominally one year, at which point the rate of degeneration appears to increase.

Two dimensional thickness maps of the ONL in a two month old wild type mouse and an age matched *Rsh1* KO mouse were processed and displayed in Figure 3-5 (b, c). Due to the manual labour required to segment the depth profiles in an entire volume, only every tenth elevation frame was extracted from the data to generate the thickness maps. In agreement with the results summarized in Table 3-1, the thickness maps in Figure 3-5 (b, c) indicate that the ONL was thinner in the *Rs1h* knockout mouse than in the wild type mouse.

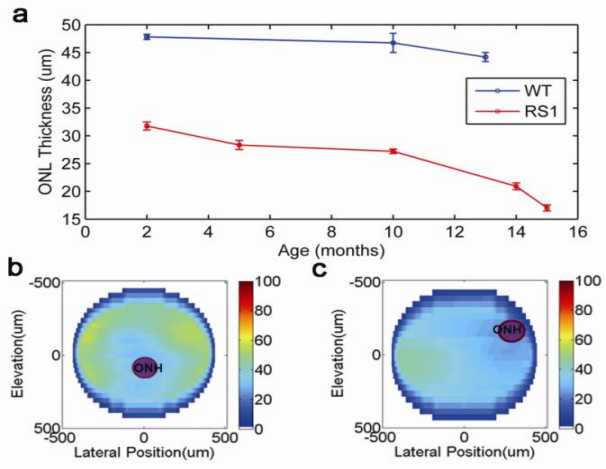

Figure 3-5: (a) ONL thickness of wild type and *Rs1h* KO mice measured with SD OCT for different age groups. Two dimensional map of the ONL thickness for (b) wild type and (c) *Rs1h* knockout mouse at two months of age. This figure was reproduced from [26], and is copyrighted by the Association for Research in Vision and Ophthalmology.

3.3 Conclusion

Non-invasive SD OCT imaging of the sub-surface retinal layers has been used to measure the thickness of the ONL in mice with retinal degeneration. In this study, we concentrated on the use of cost-effective and portable equipment for the SD OCT system. We compared the thickness measurements of the ONL in wild type mice to thinning of the ONL in *Rs1h* knockout mice, the model for X-linked Juvenile Retinoschisis. Comparison of the non-invasive SD OCT measurements to histology demonstrated a strong correlation, and the measurement results matched within experimental uncertainty. At two months of age, the ONL layers in the *Rs1h* knockout mice had thinned down to nominally seventy percent of the wild type thickness. By an age of fifteen months, the thickness of the ONL layer in Rs1H KO mice was nominally a third of the wild type. SD OCT also provided non-invasive images of the general disorganization of the retinal cell layers in the *Rs1h* knockout mice, and was also able to image holes in the INL associated with the deficiency of retinoschisis.

The disorganization of the retinal layers in the *Rs1h* knockout mice made it difficult to establish definite boundaries of the ONL, which added to the measurement uncertainty of this study. These issues are present in both the

histological and SD OCT measurements; however the ability to average over multiple images using SD OCT presents a definite advantage of the non-invasive technique.

The strength of the non-invasive technique is that it permits time course studies of retinal degeneration. In the next chapter, a drug development study using a rat model of glaucoma is presented using SD OCT to measure gradual thinning of the retina.

4. SD OCT FOR A DRUG DEVELOPMENT STUDY OF A RAT MODEL OF GLAUCOMA

4.1 Introduction

Optic nerve diseases can be classified as chronic (i.e. glaucoma) or acute (i.e. traumatic optic nerve neuropathy). Both types of these diseases are related to the death of the retinal neuronal cells called the Retinal Ganglion Cells (RGCs). The neurons are highly specialized cells, which mean that after the death of a neuron, the pathological change in the retina becomes irreversible.

Glaucoma is one of the leading causes of blindness. It is chronic and progressive neurodegenerative disease which is often concomitant with elevated intraocular pressure (IOP). A different optic nerve neuropathy is the transaction of the optic nerve (ON), which represents an acute and very rapid neurodegenerative process, also known as “ON axotomy” [31][32][33].

Pharmacological treatments are being developed to protect the structure of the retinal neuronal layers and delay RGCs death. SD OCT was investigated

in this study to measure the structural changes in the retina non-invasively and evaluate the potential benefits of a new drug in rat models of glaucoma.

4.2 SD OCT imaging of Glaucomatous Retinal Degeneration in Rats

The objective of this study was to use SD OCT to monitor if the RGCs death and GCL thinning were related. GCL is a just single layer that consists of RGCs. In histology, the NFL, GCL, and IPL can be easily observed, shown in Figure 4-1 (a). However, even with the image resolution and contrast of a laboratory grade SD OCT system, the resolution is not high enough to distinguish GCL, and IPL in rats regularly. The death of RGCs would not affect IPL, and any changes to the NFL are also relevant to the study because it is where the RGC cell bodies and the projecting RGC fibers are located. Therefore, the combination of the NFL + GCL +IPL (herein termed “NGI”) layers was measured for this study. Figure 4-1 (c) presents an overlaid image of histology and OCT image with correlated layers labelled.

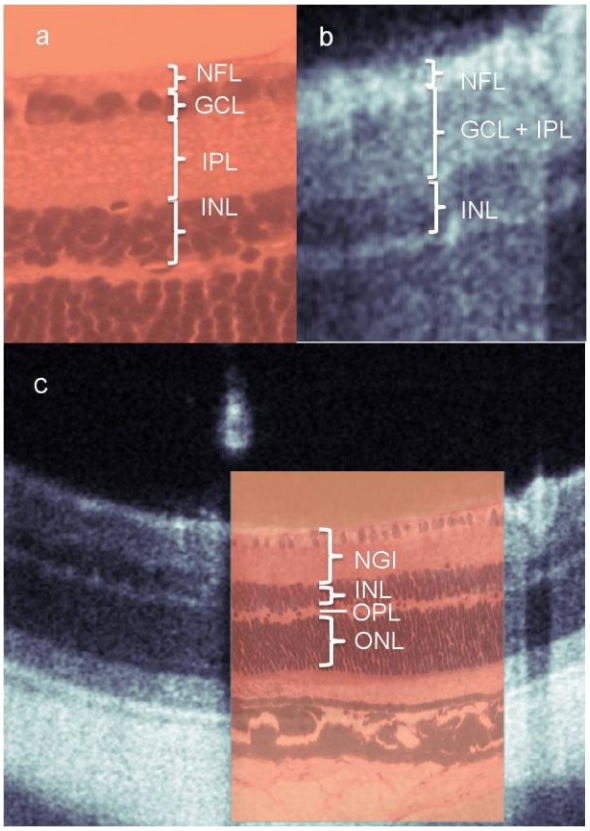

Figure 4-1: (a) Histology with observable NFL, GCL and IPL (b) Unobservable GCL and IPL in an OCT image. (c) An OCT B-scan overlaid by a histology, NGL is labelled. This OCT image was generated by averaging 5 B-scans acquired at the same location.

The optic design used in this experiment was the same as presented in Chapter 2 except that the second lens of the beam expander was replaced by a 45mm focal length lens, providing a 343μm depth of focus. This depth of focus is only slightly larger than that used for mouse imaging, but generated superior images in the rat eye.

The OCT thickness results were compared with RGC counts done by Yujing Bai in Lady Davis Institute-Jewish General Hospital. Yujing Bai also performed the glaucoma operations and participated in the statistical analysis.

4.3 Experimental protocol

All of the animal procedures abided by the IACUC and ARVO guidelines for use of animals in research, and adhered to protocols approved by McGill University Animal Welfare Committees.

For this study, one of two microsurgical procedures inducing glaucoma-like retinal degeneration was performed on the right eye of experimental rats, leaving the contralateral eye as a control. For each type of retinal degeneration, 6 rats were used, and each eye was used as an individual point in statistics. The normal group consisted of the SD OCT measurement from 6 normal left eyes, corresponding to a sample size of N_{normal} = 6 eyes. The optic nerve transaction (axotomy microsurgery [34]) was performed on the right eye (OD) of 6 rats. Three of them were treated with a neuroprotective drug after the procedure, making an axotomy sample size of $N_{axotomy}$ = 3 and a drug treated sample size of $N_{treated}$ = 3. The axotomy procedure is a highly accelerated experimental model of glaucoma,

causes ~90% RGCs loss in 14 days [36]. This first group of rats is referred to as the Axotomy group.

A second group of six rats was used to investigate the effects of the treatment on a different glaucoma model, made by performing episcleral vein cauterization [35], with the same sample group sizes. The cauterization causes the rat IOP to increase which subsequently leads to RGC death. The progression of retinal degeneration in this experimental modal is much slower which causes 3-4% RGCs loss per week. After six weeks of the procedure, about 70% RGCs remain [35]. This group of rats is referred to as the Glaucoma group.

Drug treatments were done with the experimenters blinded to treatment code. For the glaucoma model the test intraocular injections were performed at days 14 and 21 after cauterization; and the endpoint was at day 42 of high IOP. Thus, in this paradigm there is pre-existing damage for 14 days before treatment. For the axotomy model test intraocular injections were performed the day of ON transection; and the endpoint was at day 7 or 14. At the endpoint, the animals were euthanized and the eyes were enucleated for histology.

Although SD OCT imaging is non-invasive and entirely painless, the rats were anesthetized prior to imaging to minimize motion. The pupils were dilated using a topical solution (Atropine sulphate 1%, Alcon). After anesthetization, the rats were placed on a homemade stand, and gentle manual manipulation was used to rest the head of the rats in an orientation where the angle of the eye was properly coupled to the optical beam. Refraction of light at the cornea was cancelled by placing a flat coverslip coated with an artificial human tear gel over the eye. Alignment of the optical system to the rat retina required several minutes, and was followed by rapid acquisition of data, requiring nominally 10 seconds per volume.

The retinal thickness measurements were extracted by post processing saved volumetric data. In each eye, 3-4 volumes in different retina quadrants were acquired, depending on the position of the rat eyes and optic nerve head. A 3D reconstruction of a rat retina with 400 B-scans is shown in Figure 4-2 (a). From each volume, six B-scans were randomly selected at a distance of ~1.5 mm from the optic nerve head, shown in Figure 4-2 (b, c). In each B-scan, four measurements of NGI thickness were taken, shown in Figure 4-2 (c). The average of the 4 measurements was recorded as the thickness of this B-scan. A

total of seventy-two measurements of the NGI thickness were thus performed for each eye.

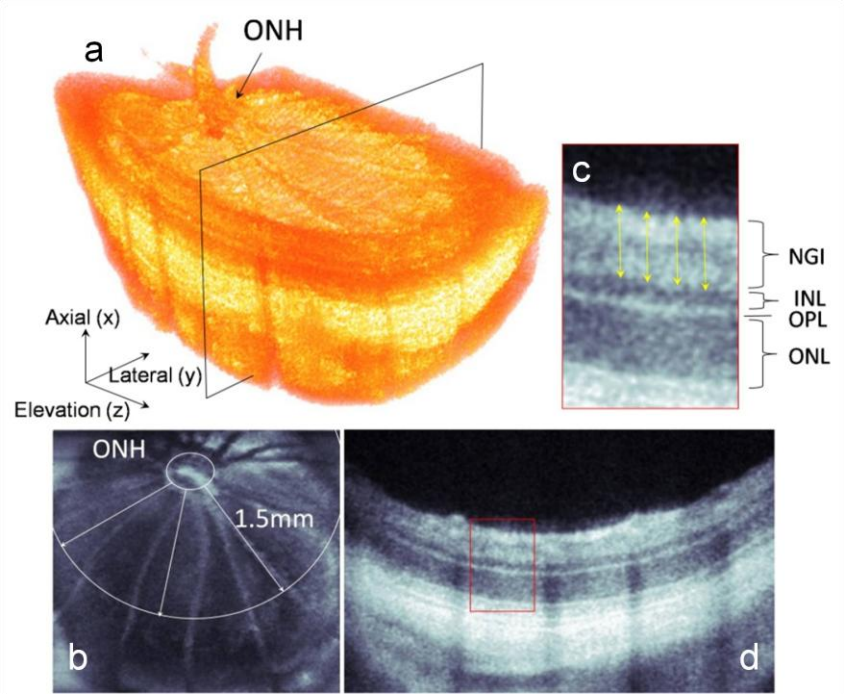

Figure 4-2: (a) 3D reconstruction of a rat retina. A single isolated B-scan (rectangle) shows the z-axis with the inner segment at the top. (b) An fundus image of the volume. Six B-scans were randomly selected at a distance of ~1.5 mm from the optic nerve head, given the red box in (d). (c) The expaned view from the red box in (d), and four measurements of the NFL-GCL-IPL (NGI) thickness were completed (yellow arrows). (d) A representative B-scan.

4.4 Results

For this study, the axotomy group was imaged for 5 times in 2 weeks with the interval of 3 days, and glaucoma group was imaged once a week for 6 weeks. Figure 4-3 shows the representative data in axotomy group which the yellow

arrow was indicated as the NGI thickness. In the untreated axotomy sample, the significant progressive loss of NGI thickness was observed from the first day of the experiment to the end point, compared with the drug treated sample. In the normal sample, the changes were not distinguishable.

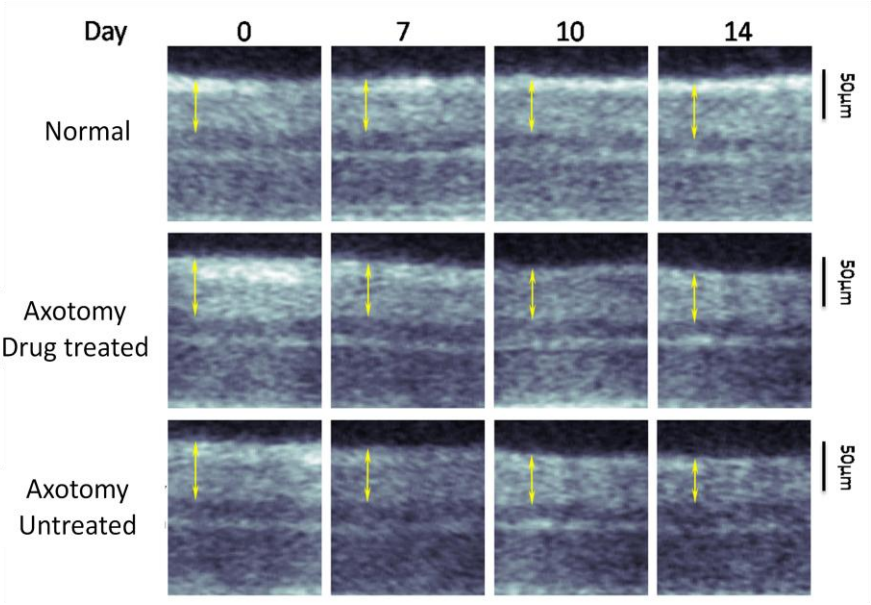

Figure 4-3: Representative sections of B-scan images for normal, axotomy, and axotomy with drug. The images are averaged over 8 frames. Note the progressive loss of NGI thickness over time, particularly in the untreated axotomy sample.

4.4.1 NGI Thickness Measurements with FD OCT

Figure 4-4 and Figure 4-5 summarizes the statistic changes in axotomy and glaucoma group. In Figure 4-5, the combined thickness of NGI in normal retinas is 71 ± 0.6 μm. At the end of the axotomy experiment the NGI thickness is

54.7 ± 1.15 μm, while for the drug treated group it was 60.8 ± 0.33 μm. In Figure 4-5, at the end of the glaucoma experiment, the NGI thickness was 51.2 ± 2.6 μm, while for the drug treated group it was 60.4 ± 0.13 μm. The results demonstrated that the drug treatment protected the structure of the retinal neuronal layers.

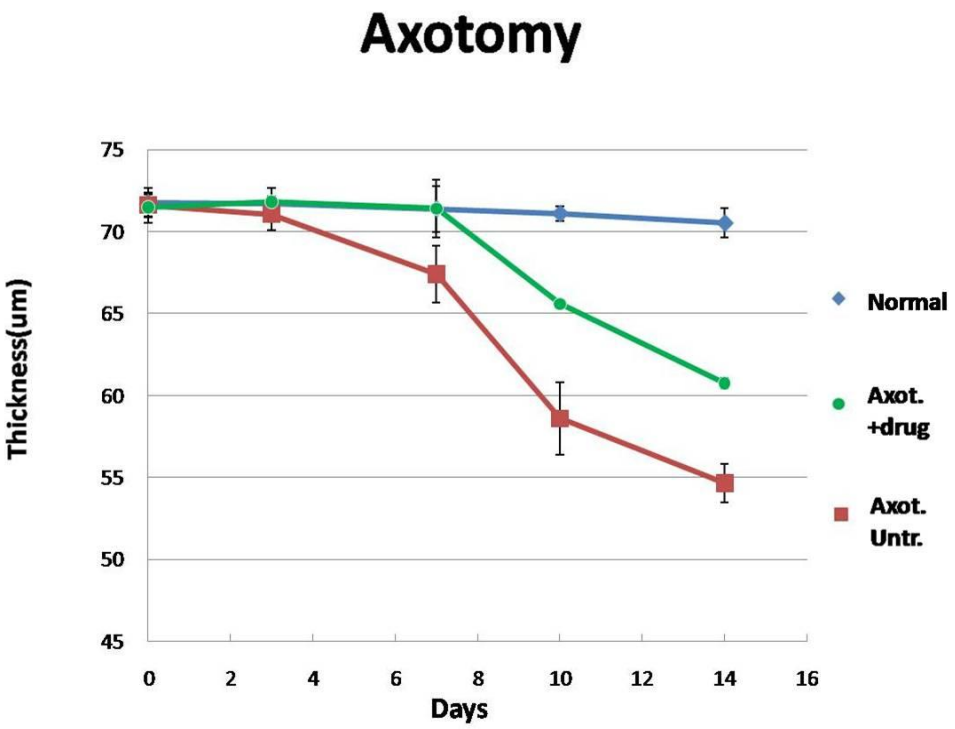

Figure 4-4: Axotomy, time-dependent (days) changes to average NGI thickness.

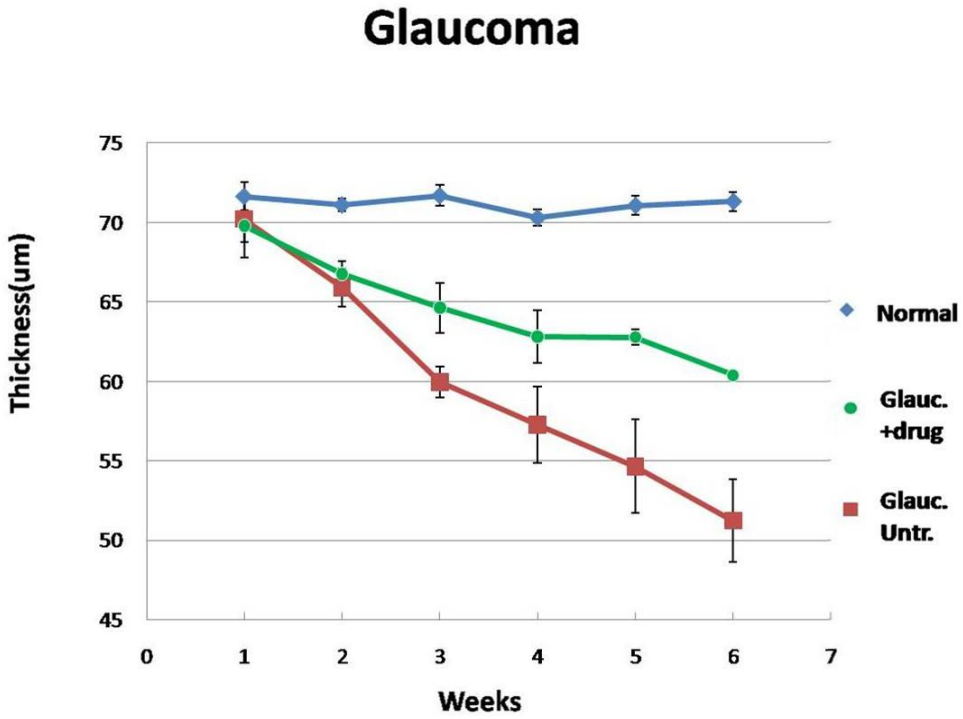

Figure 4-5: Glaucoma, time-dependent (weeks) changes to average NGI thickness.

Figure 4-6 presents the distribution of NGI thickness results from each individul rat in the glaucoma group. Figure 4-6 (a) and (b) show the results from 3 rats in which the OS were normal and OD were drug treated. The measurements at week 5 and 6 for Rat 1 were not recorded because it accidently passed away while under anesthesia. Figure 4-6 (c) and (d) show the results from the other 3 rats in the glaucoma group in which the OS were normal and OD were untreated.

The analysis of the results in Figure 4-6 indicates that the average error for measuring the retinal thickness in the control eye (OS) of the same rat over

the six week study is similar to the inter-rat variation over the same period, ~0.9μm. For the glaucoma induced eyes (OD), the retinal degeneration followed a similar trend for the three animals in a group, but had higher variation between animals. This is likely due to the variations in rate of degeneration between rats.

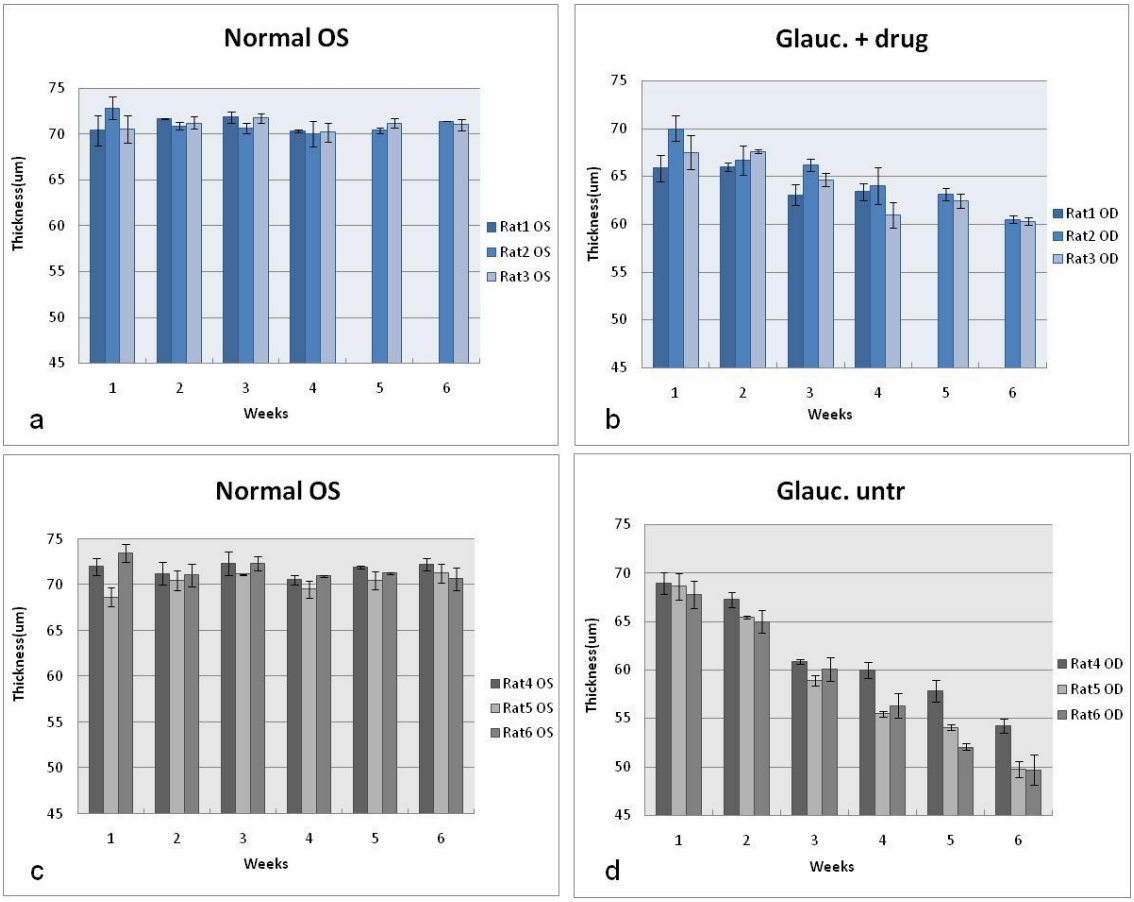

Figure 4-6: The distribution of NGI thickness results from individual rat in glaucoma group. (a) Normal OS and (b) glaucoma drug treated OD of Rats 1-3. (c) Normal OS and(d) glaucoma untreated OS of Rats 4-6.

The measurements from the axomotmy group are summarized in Figure 4-7. As for the glaucoma group, the data presented is the distribution of NGI

thickness measurement from each individul rat. Figure 4-7 (a) and (b) show the results from 3 rats in which the OS were normal and OD were drug untreated. Figure 4-7 (c) and (d) show the results from the other 3 rats in the axotomy group in which the OS were normal and OD were treated (note that the numbering of

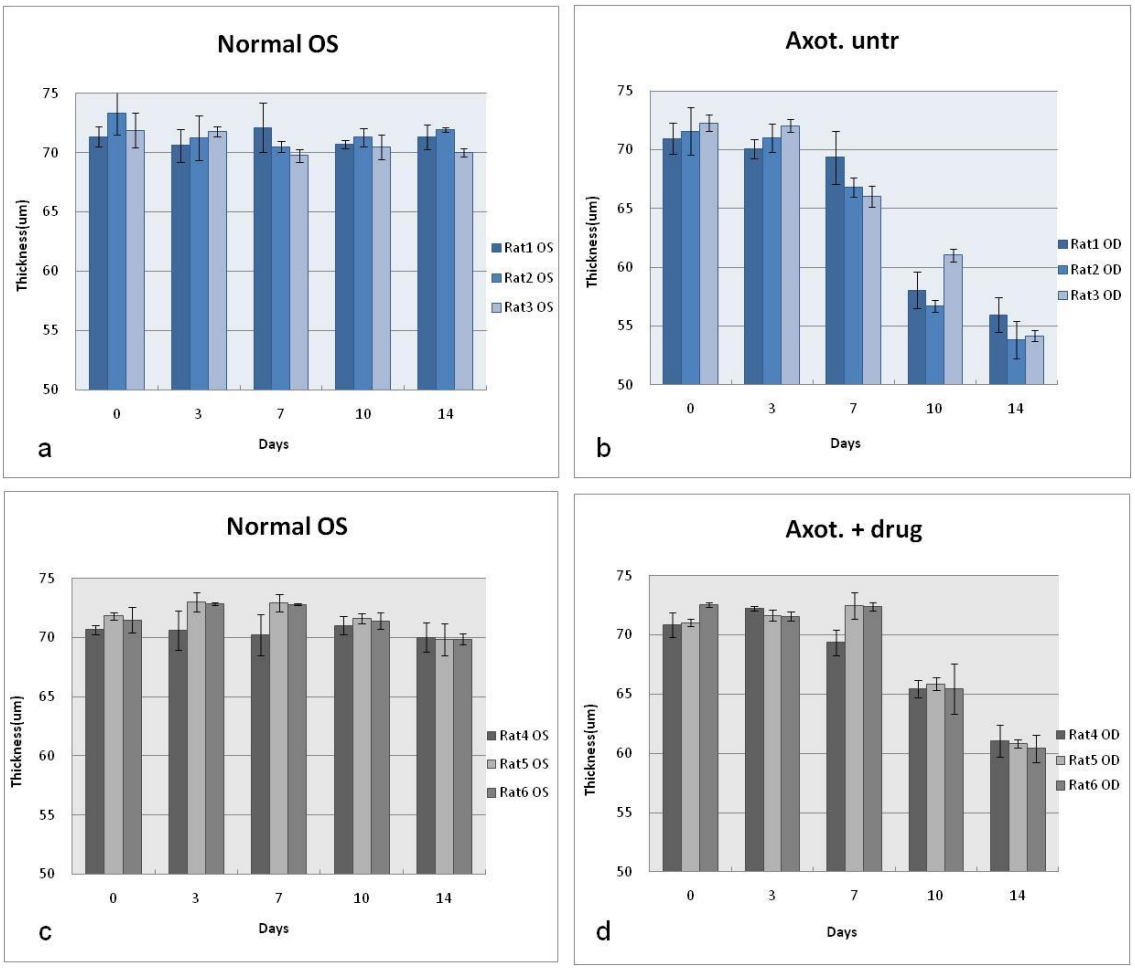

Figure 4-7: The distribution of NGI thickness results from individual rat in axotomy group. (a) Normal OS and (b) axotomy untreated OD of Rats 1-3. (c) Normal OS and (d) axotomy drug treated OD of Rats 4-6.

the rats is different between the axotomy and the glaucoma experiments). The amount of intra- and inter-rat variation in the control eyes from the axotomoy group was ~1μm, similar to that of the glaucoma group.

4.5 Discussion

SD OCT is also a useful tool to monitor the three-dimensional structural changes of the retina in longitudinal studies. Some of these relevant structural changes include the optic nerve head structure, retinal vessel diameters and retinal thickness. Unlike histology, SD OCT can diagnose and monitor effects of certain retinal degenerative diseases *in vivo*.

The symptoms of a lot of retinal degenerated diseases are usually known. For example, in the late stage of glaucoma, the vessel diameters are significantly smaller [40], and the pattern of the blood vessel far from the ONH appear bent. Figure 4-8 and Figure 4-9 demonstrate the diagnostic ability of SD OCT for morphological changes to the rat retina used in the glaucoma study. Figure 4-8 shows the *en face* projections (fundus reconstructions) of the retina wherein the differences between blood vessel pattern and diameter in a normal and glaucomatous rat can be observed.

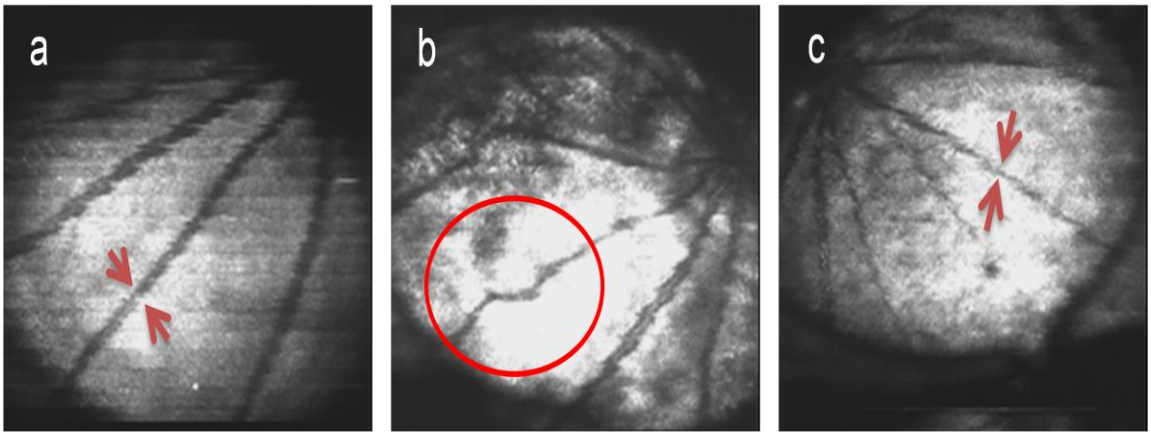

Figure 4-8: (a) A normal rat eye. (b) A forty-two days glaucoma rat with bend blood vessel. (c) A forty-two days glaucoma rat with thin blood vessel.

Another representation of glaucoma pathology observed in the rat study was the morphological change of the ONH as shown in Figure 4-9. The ONH appears to bulge forward from the retinal plane in the normal eye, and atrophy can be seen as the region around the ONH (peripapillary tissue) as the glaucoma progressed. The result is a bowed appearance of the ONH in rats with more advanced glaucoma.

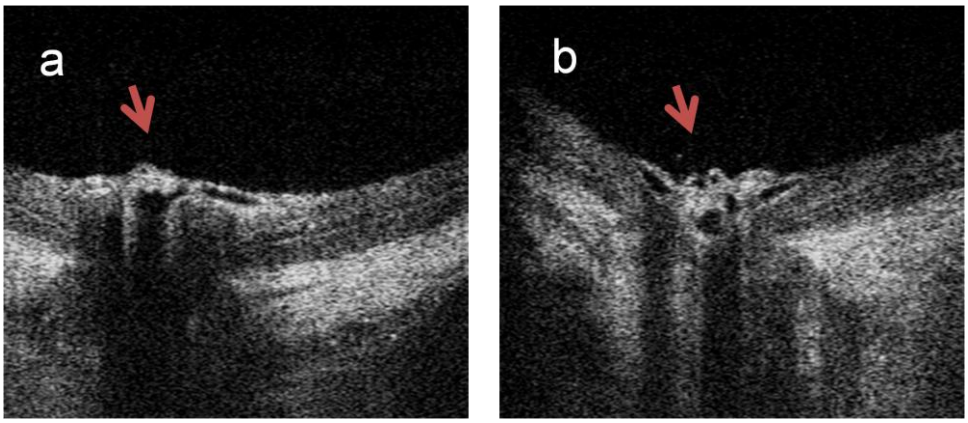

Figure 4-9: (a) Normal ONH with protuberant shape. (b) atrophy of retinal tissues around the ONH were observed in the glaucoma rat

In this study, the SD OCT imaging identified some unexpected structural changes during the experiment. Without OCT, researchers were not aware if the surgery to induce the degeneration model of glaucoma was successful, or if the neuroprotective drug was injected correctly until the end of the experiment. In Figure 4-10, detachment between RPE and choroid was found three days after the optic nerve transection procedure. The trauma might have been a cause of uncontrolled hand movements in the procedure. The early identification of the unusable data point would permit rapid correction to the experimental procedure.

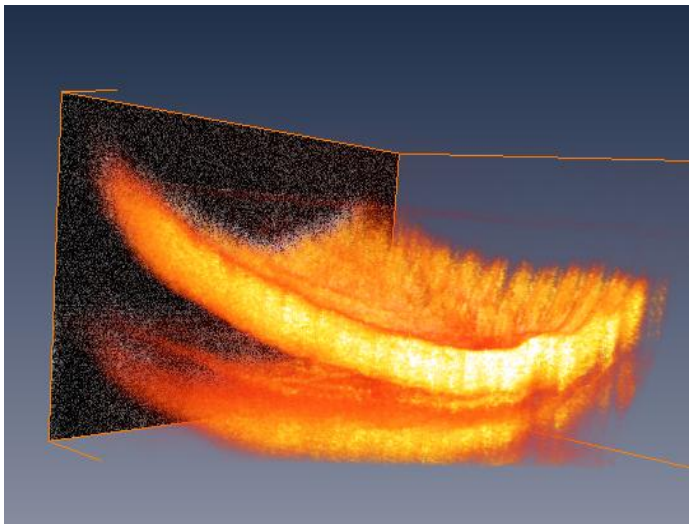

Figure 4-10: 3D volumetric view of detached retina layers

Figure 4-11 presents four observations of rat retina by using SD OCT. The drug treatment in this experiment was provided by intraocular injection. The red circle in Figure 4-11 (a) was the trace left after the injection. The white dots were considered as the drug reaction shown in Figure 4-11 (b). The squeezed layers shown in Figure 4-11 (c) was where the vessel cauterization was performed. The holes caused by retinal degeneration were observed in (c) and (d).

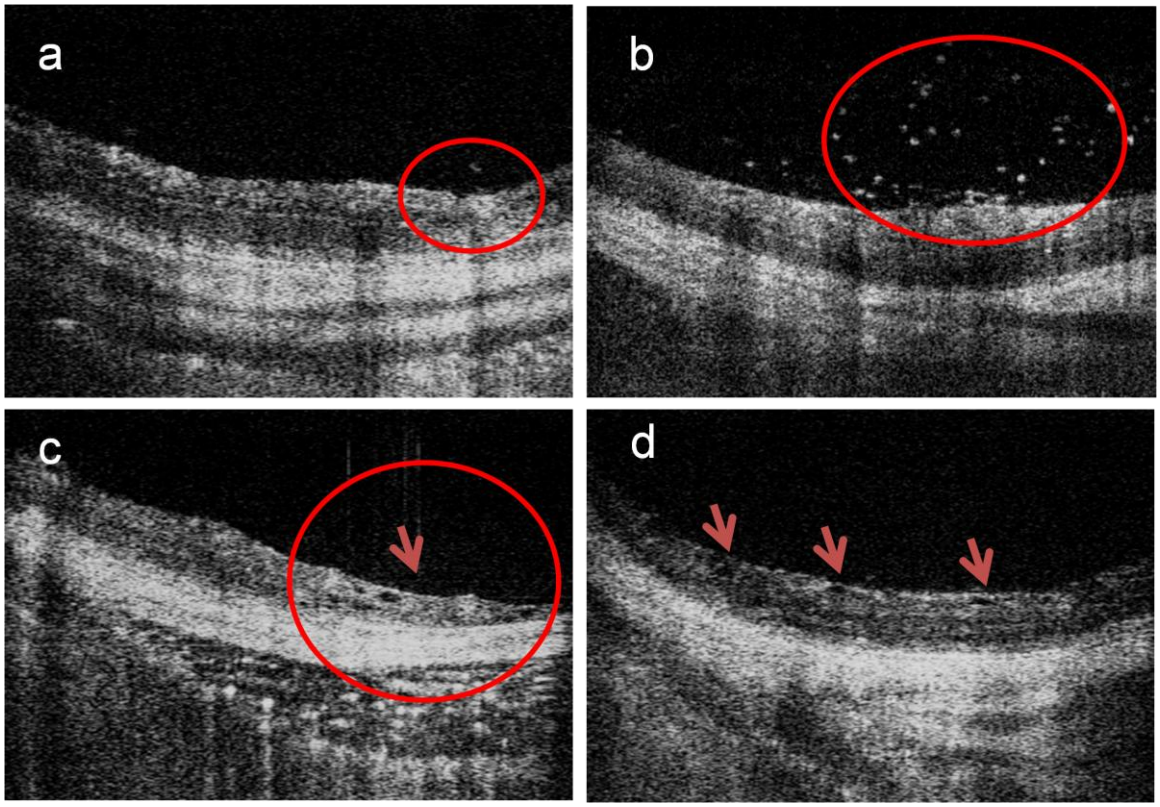

Figure 4-11: (a) Intraocular Injection mark. (b) Drug reaction. (c) Effect after cauterization performed. (d) Visible holes.

4.6 Conclusion

Non-invasive SD OCT imaging was used to conduct a longitudinal study on Glaucom rat models to measure the thickness change (NGI) caused by the death of the RGCs. We compared the thickness measurements of NGI in normal rats to thinning of the NGI in untreated and drug-treated group of both axotomy and glaucoma models. At the end of the axotomy experiment, the NGI thickness of the drug treated group was ~6μm thicker than that of the untreated group, and ~10μm thinner than that of the normal group. The glaucoma experiment also

followed a similar pattern of degeneration. For the glaucoma group, the final NGI thickness of the untreated group was ~3μm thinner than that of the axotomy untreated group. These results indicated that the drug treatment can protect the structure of the retinal neuronal layers, but are not fully protective. This might be due to the continuous stress suffered by these rat eyes and low treatment frenquency and dose.

The results presented in this chapter demonstrated the utility of SD OCT for a time course study of drug development for neuroprotection in rat models of glaucoma. In the next chapter, the validation of SD OCT measurements of retinal degeneration in *Xenopus laevis* tadpoles for the first time is presented.

5. THE VALIDATION OF SD OCT MEASUREMENTS OF RETINAL DEGENERATION IN *XENOPUS LAEVIS* TADPOLES

Transgenic animals are important to study retinal degenerative disease. The frog species *Xenopus laevis*is commonly used as a laboratory animal. The *X. laevis* retina has a rod/cone photoreceptor ratio similar to that of humans making it an excellent animal model to study retinal degeneration [41]. SD OCT imaging was used to non-invasively image retinal degeneration of the rod outer segments in a transgenic *X. laevis* tadpole model. The results demonstrate that FD-OCT is a valuable system for screening and monitoring retinal degeneration in *X. laevis* tadpoles.

5.1 Methods

The basic components of the SD OCT are the same as used for mouse and rat imaging. The difference was that the sample arm was redesigned for tadpole eye to provide a depth of focus of ~70μm. The depth of focus of the interrogating beam approximately matched the thickness of the tadpole retina,

permitting the visualization and measurement of all the retinal layers *in vivo*. The optical power incident on the eye was adjusted below 770μW, which is in accordance with the ANSI recommended limit for ocular exposure in humans.

Prior to SD OCT imaging, tadpoles were anesthetized by immersion in tadpole rearing medium (Ringer's solution) containing 0.01% tricaine methanesulfonate (Sigma-Aldrich) for 1-2 minutes. The anesthetized tadpoles were transferred to a stage soaked in Ringer's solution to prevent them from drying out during the course of SD OCT imaging. Imaging was performed quickly, with alignment and acquisition requiring nominally five minutes per specimen.

Volumetric images were acquired by raster scanning the SD OCT beam across the eye, and reconstructions were generated using Amira (Visage Imaging). The rapid image acquisition rate also permitted the acquisition of multiple frames at single position for averaging. The two-dimensional B-scans presented in this manuscript were generated by averaging 40 frames to reduce speckle. No further post-processing was performed. Histology images were acquired by Dr. Damian Lee (UBC/VGH Ophthalmology and Visual Science) using Zeiss 510 Meta laser scanning confocal microscope (Carl Zeiss).

All procedures were performed in accordance to the ARVO Statement for the Use of Animals in Ophthalmic and Vision Research.

5.2 RESULTS

5.2.1 SD OCT retinal scans of *X. laevis* tadpoles.

SD OCT was used to image wild-type *X. laevis* tadpole retina at various stages of development, from Nieuwkoop-Faber developmental stage 46/47 to stage 55/56 [48]. Cross-sectional images of the *X. laevis* tadpole eye were acquired as shown in Figure 5-1. Although the light was focused on the retina, the cornea and iris were also easily identifiable in the SD OCT images, allowing for reconstruction of the anatomy of a normal tadpole eye. The source of contrast in SD OCT is the intensity of reflected light of tissue boundaries as well as the relative amount of backscattered light between different tissues. In the retina, the plexiform layers and the RPE backscatter strongly and appear white, whereas the nuclear layers scatter weakly and appear darker.

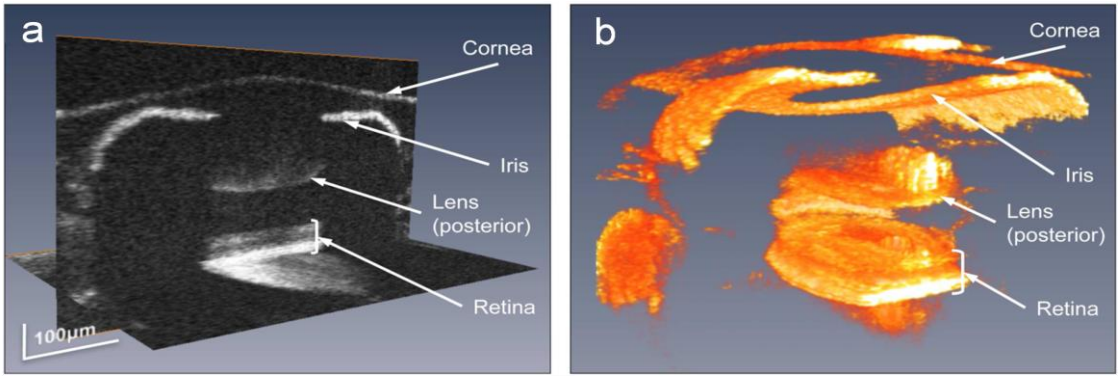

Figure 5-1: SD OCT images of a normal tadpole eye. (a) 2D cross-section view and (b) 3-D volumetric view of the tadpole eye. Tissues that have high optical reflectivity (e.g., iris and retinal pigment epithelium) appear bright in the images, while tissues that backscatter less (e.g., lens) appear dark. Scale bars, 100μm. This figure was reproduced from [47], and is copyrighted by the Association for Research in Vision and Ophthalmology.

The optics in the SD OCT sample arm were customized to a shorter depth of focus than used for rodent imaging because of the comparatively thinner retina of the tadpoles. The lenses used are listed in Table 2-1. SD OCT B-scans of the tadpole retina showing the distinct banding pattern of the retinal layers are presented in Figure 5-2. The individual retinal layers were identified by comparing the cross-sectional SD OCT images with the histological sections.

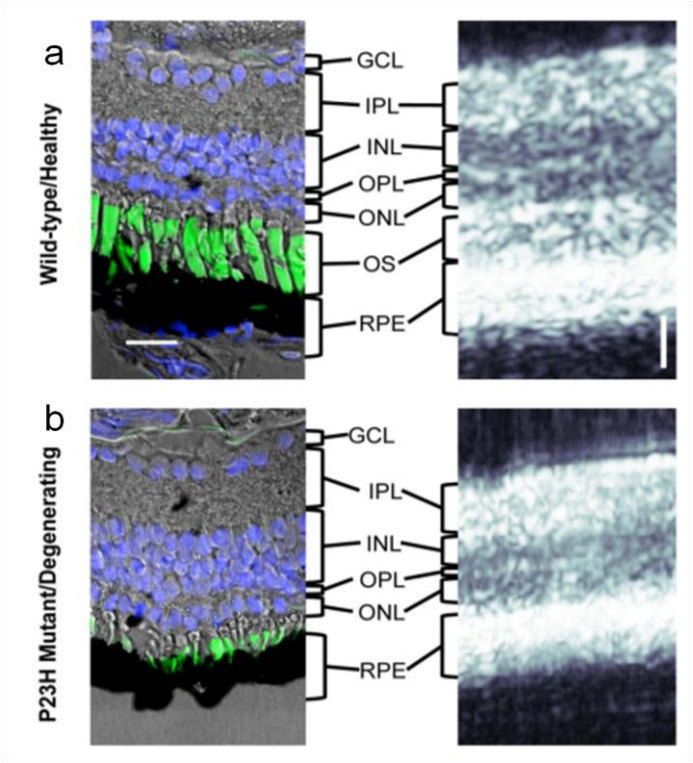

Figure 5-2: Comparison of tadpole retina images from histology and SD OCT. (a) healthy wild-type retina and (b) degenerating transgenic retina expressing rhoP23H. Scale bars, 20µm. This figure was reproduced from [47], and is copyrighted by the Association for Research in Vision and Ophthalmology.

In both clinical and research settings, SD OCT can be used as a diagnostic tool to image *in vivo* morphological changes in degenerating retinas. To assess the ability of SD OCT to detect differences between normal and degenerating tadpole retinas, SD OCT retinal scans from transgenic tadpoles and wild-type animals were compared.

Table 5-1 shows the thickness of the INL and OS as measured from histology and SD OCT. The OS layer in the tadpole mutant retina was significantly thinner than the wild-type retina in both measurements.

Table 5-1: Thicknesses (in μm) of inner nuclear layers (INL) and outer segments (OS) measured from histology and OCT. (n > 7, mean ± S.D.).

	Histology		OCT	
	INL	OS	INL	OS
Wild-Type	25.3 ± 3.5	24.9 ± 4.4	20.10 ± 2.3	15.3 ± 1.3
Transgenic	25.9 ± 2.6	6.7 ± 3.3*	19.85 ± 2.3	5.7 ± 2.4*

The relative thickness of the retina (the INL+ ONL+OS thickness normalized to the thickness of the entire retina) from both histology and SD OCT were also measured. The relative thickness of the transgenic (degenerated) retina was significantly less than the control wild-type retina in both the histological sections and SD OCT scans in Figure 5-3. The percent decrease measured from both histology and SD OCT was 13±1%. These measurements indicate that the interpretation and assignments of the retinal layers in SD OCT images are consistent, and that SD OCT is capable of detecting the thinning of rod OS in the degenerating mutant tadpole retina.

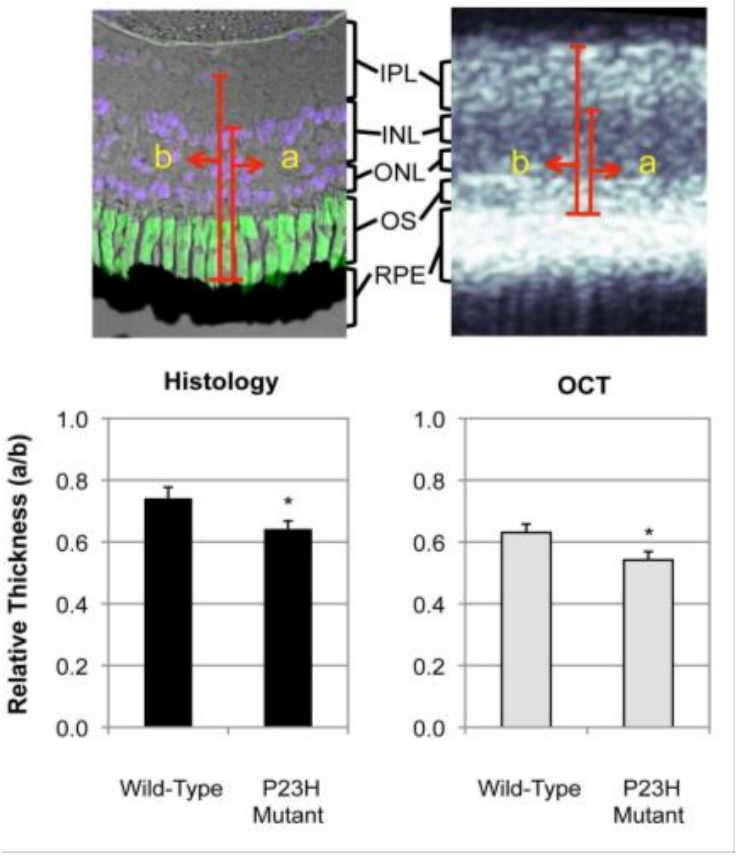

Figure 5-3: Relative thickness of wild-type and transgenic retinas as measured from histological sections (left) and FD-OCT (right) (n > 7, mean ±S.D.). From both measurements, the relative thickness of the mutant retina is significantly thinner than the wild-type control. This figure was reproduced from [47], and is copyrighted by the Association for Research in Vision and Ophthalmology.

5.2.2 *In vivo* imaging of progressive retinal degeneration in *X. laevis* larvae with SD OCT

To assess the utility of SD OCT for imaging progressive retinal degeneration in a given tadpole, a drug-inducible *X. laevis* model of retinal degeneration that allows rapid induction of rod cell over 5 days was used [51]. SD OCT was used to monitor the retina of tadpoles before administering the drug

and at two time points after drug administration. At each time point, a subset of tadpoles was euthanized for histology. Figure 5-4 shows representative images of tadpole retinas at three time points: immediately before, 2 days after and 4 days after administration of the drug. Before exposure to the drug, the INL, ONL, OS and RPE can be observed from SD OCT, in the pattern of a healthy retina. Two days after drug exposure, histology showed that the majority of rods were smaller and dead rod OS bodies were seen within the RPE. The disruption in the RPE layer in OCT images indicates a change in reflectivity and backscatter in the RPE, consistent with the accumulation of phagosomes in the RPE. Four days after drug exposure, relatively few phagosomes were observed in the RPE in histology. The OS layer could not be identified in SD OCT retinal scans of 4 days post-drug tadpoles, and the RPE appeared as a featureless single layer. These data demonstrate that SD OCT is able to image intermediate rod degeneration as well as phagosomes in the RPE *in vivo*.

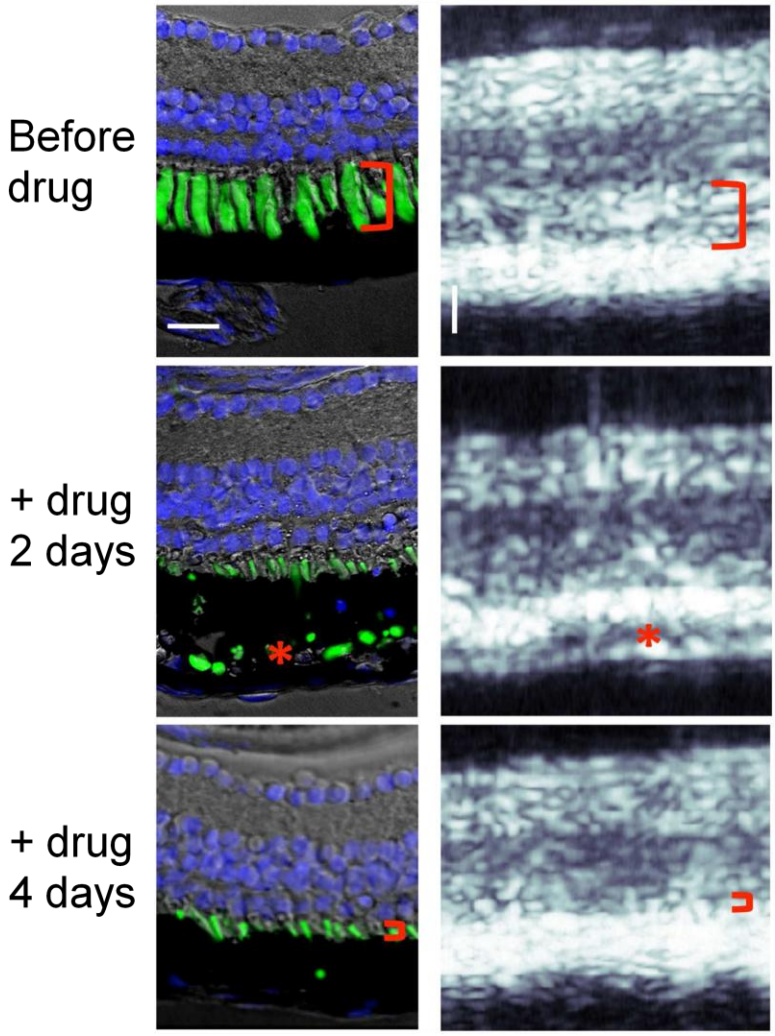

Figure 5-4: *In vivo* imaging of the progression of retinal degeneration. Laser scanning confocal micrographs (left panels) and SD-OCT images (right panels) show progressive retinal degeneration over a period of 4 days after induction of cell death. On day 2 post treatment, the disruption in the RPE from OCT indicates a change in reflectivity and backscatter, consistent with the accumulation of phagosomes in the RPE (red asterisk). By day 4 post drug, the rod OS was completely ablated (red bracket). Scale bars, 20µm. This figure was reproduced from [47], and is copyrighted by the Association for Research in Vision and Ophthalmology.

5.3 Discussion

For the first time, SD OCT was applied to image *X. laevis* tadpole retina *in vivo.* The same retinal structures were observed with OCT and with histology. A longitudinal study of degenerating retina was performed and the progressive loss of rod outer segments *in vivo*. The results demonstrated the ability of SD OCT to perform time course studies of retinal disease progression in individual transgenic *X. laevis*.

Histology introduces artifacts such as shrinkage of the tissue during fixation. The *in vivo* SD OCT measurements of retinal layers showed less variation compared with measurements of histological sections. Taking into consideration the potential artifacts from histological processing, it was expected that the SD OCT measurements would be more consistent.

One inherent limitation of SD OCT imaging is its maximum resolution. While SD OCT can resolve the major retinal layers, histology is still required for single-cell resolution and analysis. Furthermore, histological analysis has the advantage of the ability to label specific cells with fluorescence. However, compared with the time consuming process of histology, the speed at which SD

OCT retinal scans can be acquired non-invasively implies that SD OCT may be used to rapidly screen large numbers of tadpoles.

6. CONCLUSION

This thesis demonstrated that SD OCT is a powerful tool to identify and monitor retinal disease progression through *in vivo* volumetric imaging in laboratory animals without sacrificing them.

6.1 Summary

Throughout this research, the prototype framework of a complete, end-to-end analysis system included image acquisition, data processing, manual segmentation, thickness measurements, and statistical analysis was developed for small animal retinal imaging. The anatomy of the eyes in human and small animals is similar, but the high radius of curvature in smaller eyes makes high resolution imaging. Chapter 2 introduced a prototype SD OCT with an adjustable beam expander in the sample arm. The optical design made it easy to adapt the depth of focus for different animals. Investigation of retinal degeneration in mice using the SD OCT prototype was presented and validated against histology. The utility of SD OCT to monitor retinal degeneration in a rat model of glaucoma was

demonstrated, and showed gradual thinning of the related retinal layers. Lastly, imaging retinal degeneration in a transgenic *X. Laevis* model was validated against histology, demonstrating the utility of OCT in new animal systems.

SD OCT was used for small animals retinal imaging, and differences and difficulties were found from animal to animal. Imaging the rat and mouse requires a lot of human manipulation to locate the ONH and align the beam to the right location. Imaging the pigmented rodents is even more challenging because their eyes are dark so that locating the ONH in a limited time requires experience and luck.

The severe motion artifact was caused by breathing and heart beating and introduced the need for a lot of post processing effort. Tadpole imaging was relatively easier because the tadpole only needed to be placed on a wet “bed” and there was almost no motion during imaging. However, the tiny size of the tadpole eye and high level of aberrations made the retinal layers blurry in OCT images.

For rodent imaging, after anesthetization the orientation of the eye, and thus the ONH location, changed randomly. During the imaging acquisition, it was

difficult to align the measument to exactly same spot on the retina over mulitpe imaging sessions. Our solution was to perform all the measurements at a very close area based on the location of the ONH and blood vessels. As discussed in Chapter 4, the variation in the measurement of the control eye NGI thickness was only ~1.5%.

For our study, the thickness was calucated whithout considering the angle term, which lead to one source of error. Imaging quality was also an important source of errors. The sidelobe artifacts and the limitation of the resolution caused some blurriness in the OCT images, introducing difficulties to delieanate the boundary of the layers.

The comparison of the OCT imaging to histology was an important contribution of this research. Despite the sources of error in the OCT measurements as discussed above, there many advantages over histology. Histology suffers from the same problem as OCT of not knowing the true angle at which the section is being acquired, and this results in a small measurement uncertainty. Additional errors in histology arise from the processing steps (including freezing), that cause the retinal tissues layers to grow and shrink. Due

to the processing details, the relative change in thickness of the retinal layers is not always consistent. Furthermore, the physical processing in histology often leads to distortion of the retinal shape, which is largely preserved in non-invasive OCT imaging.

This research on OCT image acquisition in rodents is still in the early stages, and can benefit from additional efforts to improve image acquisition and processing.

6.2 Future Work

Future research topics for small animal retinal imaging will include improvements of imaging acquisition and segmentation.

6.2.1 Scanning patterns for image acquisition

Image acquisition can be improved by implementing different scanning patterns. Throughout this thesis, a raster scan approach was used for retinal imaging (as discussed in Chapter 2). Improvements to data quality can be made by incorporating averaging, or changing to a radial scanning pattern.

6.2.1.1 Averaging frames

The OCT images are highly speckled, and make it harder to visualize the small features in the retina. One method to reduce speckle would be average multiple frames, improving the image quality and permitting better visualization of the boundaries in each retinal layer. Some of the images shown in chapter 4 and 5 are averaged by a few numbers of adjacent frames. The blurriness of the layer boundary is observed because the adjacent frames were not acquired in the same position on the retina. The idea of an averaging scanning pattern is to acquire a number of B-scans at the nearly the same position (relative to lateral feature size) before moving to the next position. This will keep image integrity and reduce image blur introduced by averaging.

6.2.1.2 Orthogonal frames

As presented previously, the mice and rats were anesthetized prior to SD OCT imaging to minimize motion, but this did not get rid of the motion entirely. Figure 6-1 shows an acquired image dataset of a rat retina which is constructed into a 3D volume. Motion artifacts are observed which is likely caused by head and eye movement of the subject. The slow scan suffers severe motion artifacts due to the long acquisition time (10's of seconds). Attempts to average multiple

frames at each location will only make motion artifact worse. For rodent eye imaging, better immobilization such as a bite bar could be used to reduce the effect. However, even these will not remove the artifacts completely. Sieun Lee from BORG implemented a motion correction algorithm, and the 3D volumetric views presented in the previous chapters were motion corrected by the algorithm. It detects the boundary in slow scan (with motion) and then gets corrected by fitting a smooth curve. However, the blood vessel is appeared as an outgrowth on the surface layer can also be “flattened out”.

Motion correction can be improved by acquiring a few orthogonal scans after each acquisition. Orthogonal scans are acquired in near real time and would be a more accurate reference for aligning the slow scans for motion correction of the entire volume.

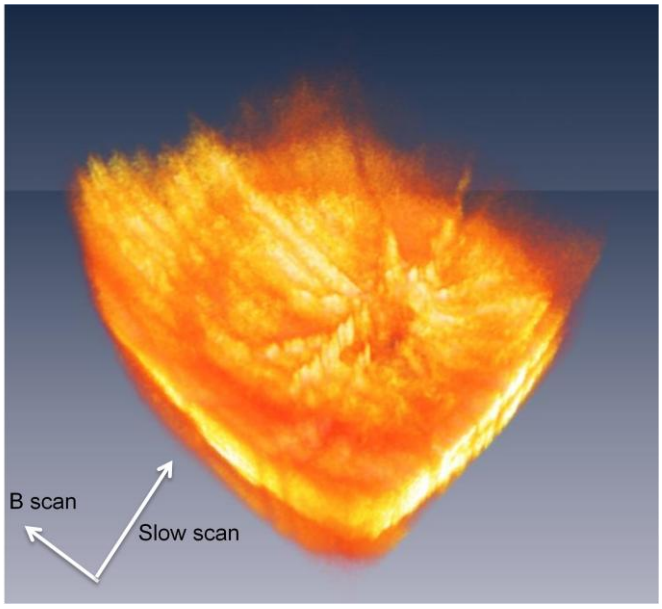

Figure 6-1: Volumetric visualization of a rat eye in Amira.

6.2.1.3 Radial Scanning patterns

Volume acquisition of 400 frames acquired ~10 seconds and encountered motion artifacts caused by breathing, or heart beating. A large number of frames provides higher resolution images of the retina, but also contains more motion artifacts. Reducing the number of scan in the same area will obviously lower the resolution of the image. To deal with this problem, a radial scanning pattern could be implemented to acquire fewer numbers of frames (e.g. 40 frames) for a similar area which only takes ~1 second, and a volume can be interpolated by these 40 radial sections. Implementing the radial scan involves considerations for

alignment which is more challenging than simple raster scanning. Furthermore, the issue of correcting motion artifacts is anticipated to be much more complex in radial scanning than in regular raster scanning.

6.2.2 Automated segmentation

In a SD OCT volume, only a few frames were segmented and measured for statistical analysis of the retinal layer thickness results. In the long run, two dimensional thickness maps (e.g. Figure 3-5 (b, c)) of the segmented measurements on a retinal volume is desired to monitor degeneration in the retina. However, manual segmentation and measurement are highly labour intensive due to the large amount of volume data acquired, making this approach not readily feasible. An option would be to apply automated segmentation technique in order to significantly reduce the amount of time and effort. Additionally, automated segmentation has the potential to eliminate human error and inter-observer variation in the delineation of the retinal layer boundaries.

In the mouse retina imaging experiment presented in Chapter 3, the disorganization of the retinal layers made it difficult to establish definite boundaries of the ONL, which added to the measurement uncertainty of this

study. With automated segmentation of the layers, the ONL thickness measurement with SD OCT can also be extended to a large area of the retina by processing the entire volume of data contained in the reconstructed fundus-type images shown in Figure 3-5 (a, b).

Currently, automated segmentation of the depth profiles in two dimensional OCT image using advanced active contour algorithms is under development by Azadeh Yazdanpanah in the BORG. The preliminary research has demonstrated promising results for segmentation of the retinal layers in normal rat eyes. Extension of the automated segmentation algorithm to 3D volumetric data will provide better performance to track degeneration in diseased eyes.

The combination of SD OCT with new scan patterns, improved averaging, and automatic segmentation will revolutionize non-invasive retinal imaging in small animals. These tools have the potential to accelerate of visual science for the development of therapies for diseases causing blindness.

APPENDICES

Appendix A: Image Acquisition

1. Preparation of equipment and instrumentation for beginning of protocol
   A. Dalsa camera
      a) Turn on the camera, make sure the cable is connected with the computer and the camera
      b) Open the Dalsa QuickCam GEV software when the local connection is connected
         i. When the dialog box with IP address pops up, click “connect”
         ii. Set variables based on user’s preference
             Default settings:
             Display->width (512)
             Exposure time (LineRate: 20000Hz)
         iii. Stop the camera, File->save to XML file to C:\overwrite DalsaGigE.XML
         iv. Close the program
   B. Scanning Galvo Mirror Systems
      a) Make sure the galvos are connected (2 cables, 1 for each mirror)
      b) Turn on the Galvo, and turn on the fan to keep it cool
         (WARNING! Galvo will break down if fan is not turned on)
   C. Sample arm & Reference arm
      a) Turn on the power meter. Make sure the black fiber is attached. The settings of the power meter are as follows:
         i. Wavelength: 820nm
         ii. Unit: microWatts
      b) Make sure there is no mirror or strong reflector standing in front of the sample arm
   D. Optical Fiber
      a) Keep optical fiber well organized. Leave enough free space for

sample imaging avoiding breaking the fiber. Handle optical fiber with care; do not bend fibers

E. Laser (Procedures are set this way in order not to damage the laser.)

a) Turn on the switch. 2 LEDs will turn red—this means that it has powered up but laser is still off

b) Proceed to press each bottom one time from left to right. LEDs will turn off which signifies that the laser is warming up

c) After a few minutes, press the leftmost button and wait for the LED to turn green. Check the value on the power meter; it should be lower than 0.020μW. Then proceed to turn the button to the right, and wait for LED to turn green

d) To turn off the laser, do the steps backward.

2. OCT Procedures

a) Open OCTViewer program shown below:

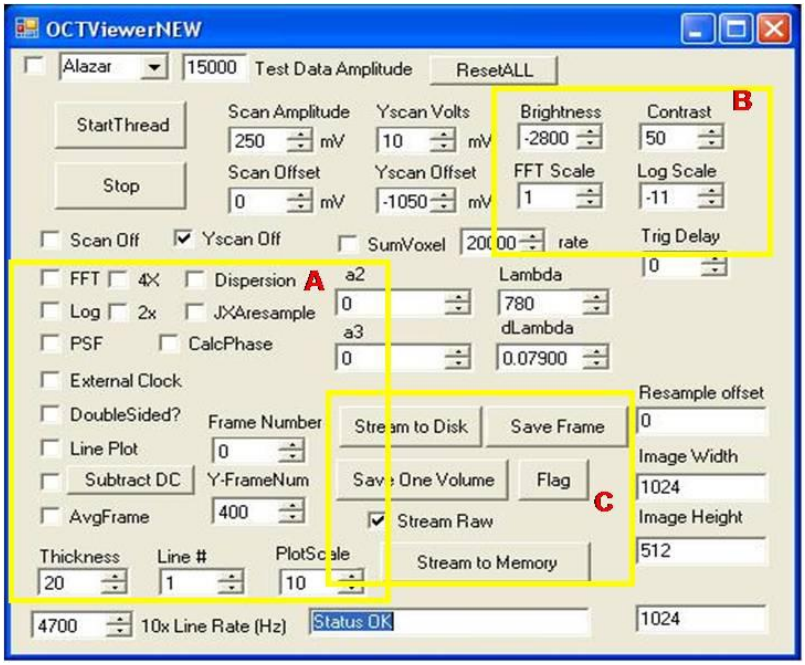

The boxed areas are discussed below.

b) Important Functions (Top Left - Bottom Right):

i. Five modes. Dalsa: Real-time imaging; Load: Load existing data

ii. StartThread & Stop:

1. Dalsa mode: First time click StartThread to start imaging system; then Stop to freeze, StartThread to continue

2. Load mode: Load the exiting file. Stop to freeze, StartThread to continue. To open a new file, check the checkbox on the very top

left, then StartThread

iii. Area A：

1. Scan Off & Yscan Off
   a) Scan Off checked: both X and Y scan off
   b) Yscan Off: Y scan off, X scan on (First time start the program, default is checked. Need to uncheck it to active scanning system)
2. Processing procedures
   a) Check the checkboxes shown below to see OCT image:
      i. FFT: Fourier Transformation
      ii. Log: Logarithm
      iii. Dispersion: Dispersion Compensation, adjust a2 and a3 to achieve sharper image while checked
      iv. Subtract DC: DC subtraction
   b) Y-FrameNum:
      i. Dalsa mode: first time start the program, the number (user defines, default: 400) of frames can be saved as a volume. The number frames must be less than 400
      ii. Load mode: Check the file size and change the number to correct number of frames and StartThread
   c) Frame Number: In Load Mode, Stop to freeze, and change the number to see corresponding frame

iv. Area B:

1. FFT scale: when dispersion is checked. Change the number to 4
2. These parameters can be played with to change the contrast and brightness

v. Area C (File saving: File name is generated automatically based on the time of acquisition):

1. Save Frame: Save single frame to \DataAcquire\Saveframe\
2. Flag: Save a volume to \DataAcquire\

vi. Sumvoxel: to see the fundus image in real time

3. System Components
   a) Setup was presented in Figure 2-4
   b) The sample arm
      i. The adjustable lens is to adjust the right focus regarding to various eye size. The other lenses are fixed

ii. Do not place a mirror as a sample. The strong back-refelection will BREAK the laser

c) The reference arm & Powermeter
   i. While moving the reference arm, always be aware of the powermeter. Don't go over 0.100μW.

d) Slit lamp
   i. Provides a joy-stick control for alignment of the OCT system to the sample. Gives up and down, forward and backward directions freedom.

Appendix B: Alignment of the small animals

Rodents (Rat and Mouse):

First, the rat or mouse need to be anesthetized using an intraperitoneal injection of ketamine and xylazine mixture (0.1ml per 10 g body weight). After anesthetization, place their body gently on a heating pad to maintain warmth, and simple manual manipulation is used to rest the head of the rat or mouse in an orientation where the angle of the eye is properly coupled to the optical beam. Before imaging, a topical solution (atropine sulphate 1%) can be used to dilate the pupils. Refraction of light at the cornea is cancelled by placing a flat coverslip generously coated with a generic artificial tear gel over the eye. Alignment of the optical system to the rat or mouse retina required several minutes. A sample figure showing the initial alignment of a (mouse or rat) to the OCT system is in Figure 2-8.

Tadpoles:

Prior to imaging, anesthetize the tadpoles by immersion in tadpole rearing medium (Ringer's solution) containing 0.01% tricaine methanesulfonate (Sigma-Aldrich) for 1-2 minutes. The anesthetized tadpoles then are transferred to a stage soaked in Ringer’s solution to prevent them from drying out during the course of imaging. Imaging can be performed quickly, with alignment and acquisition requiring nominally five minutes per specimen.

REFERENCES

[1] D. Huang, E. A. Swanson, C. P. Lin, J. S. Schuman, W. G. Stinson, W. Chang, M. R. Hee, T. Flotte, K. Gregory, C. A. Puliafito, and J. G. Fujimoto, "Optical Coherence Tomography," Science **254**, 1178-1181 (1991).

[2] J. Fujimoto, W. Drexler,Optical Coherence Tomography: Technology and Applications.Springer Berlin Heidelberg, 2008. [E-Book Series] Available: SpringerLink-Book.

[3] J. G. Fujimoto, "Optical coherence tomography for ultrahigh resolution in vivo imaging," Nat. Biotechnol. **21**, 1361-1367 (2003).

[4] W. Drexler, U. Morgner, F. X. Kartner, C. Pitris, S. A. Boppart, X. D. Li, E. P. Ippen, and J. G. Fujimoto, "In vivo ultrahigh-resolution optical coherence tomography," Opt. Lett. **24**, 1221-1223 (1999).

[5] W. Drexler, U. Morgner, R. K. Ghanta, F. X. Kärtner, J. S. Schuman, and J. G. Fujimoto, "Ultrahighresolution ophthalmic optical coherence tomography," Nature medicine **7**, 502-507 (2001).

[6] Cense, B., N. Nassif, T.C. Chen, M.C. Pierce, S.H. Yun, B.H. Park, B.E. Bouma, G.J. Tearney, and J.F. de Boer. Ultrahigh-resolution high-speed retinal imaging using spectral-domain optical coherence tomography. Optics Express. 2004; 12(11):2435-2447.

[7] Robert H. Webb, George W. Hughes, and Francois C. Delori, "Confocal scanning laser ophthalmoscope," Appl. Opt. 26, 1492-1499 (1987).

[8] Y Yassur, R Siegel, E Topper, M Karp and I Ben-Sira, Fundus photography using monochromatic light. In: S Fine and SL Owens, Editors, Management of Retinal Vascular and Macular Disease, Waverly, Baltimore (1982).

[9] W. Drexler, H. Sattmann, B. Hermann, T. H. Ko, M. Stur, A. Unterhuber, C. Scholda, O. Findl, M. Wirtitsch, J. G. Fujimoto, and A. F. Fercher, "Enhanced visualization of macular pathology with the use of ultrahighresolution optical coherence tomography," Archiv. Ophthalmol. **121**, 695-706 (2003).

[10] Glencoe Health 2nd Edition. Mission Hills: Glencoe Inc., 1989: 61.

[11] S. L. Polyak. *The retina*. Chicago: University of Chicago Press; 1941.

[12] “Simple Anatomy of Retina,” John Moran Eye Center, October 2003 [Online]. Available: http://webvision.med.utah.edu/index.html [Accessed: September 29, 2008].

[13] Kolb, H. (1991) The neural organization of the human retina. In "Principles and Practices of Clinical Electrophysiology of Vision" (Eds. Heckenlively, J.R. and Arden, G.B.) Mosby Year Book Inc., St. Louis, pp. 25-52.

[14] Leo M. Chalupa and Robert W. WilliamsEye, “Retina, and Visual System of the Mouse”. Sample Chapters Online Available: http://mitpress.mit.edu/catalog/item/default.asp?ttype=2&tid=11633c

[15] Srinivasan, V. J., T. H. Ko, et al. (2006). "Noninvasive volumetric imaging and morphometry of the rodent retina with high-speed, ultrahigh-resolution optical coherence tomography." Invest Ophthalmol Vis Sci **47**(12): 5522-8.

[16] Weber, B.H., H. Schrewe, L.L. Molday, A. Gehrig, K.L. White, M.W. Seeliger, G.B. Jaissle, C. Friedburg, E. Tamm, and R.S. Molday. Inactivation of the murine X-linked juvenile retinoschisis gene, Rs1h, suggests a role of retinoschisin in retinal cell layer organization and synaptic structure. Proc Natl Acad Sci U S A. 2002; **99**(9):6222-7.

[17] Maciej Wojtkowski, Vivek Srinivasan, Tony Ko, James Fujimoto, Andrzej Kowalczyk, and Jay Duker. “Ultrahigh-resolution, high-speed, Fourier domain optical coherence tomography and methods for dispersion compensation.” Optics Express, Vol. 12, Issue 11, 2404-2422 (2004).

[18] D. X. Hammer, A. J. Welch, G. D. Noojin, R. J. Thomas, D. J. Stolarski, and B. A. Rockwell, "Spectrally resolved white-light interferometry for measurement of ocular dispersion," J. Opt. Soc. Am. A. Opt. Image Sci. Vis. **16**, 2092-2102 (1999).

[19] S. Jiao, C. Wu, R. W. Knighton, G. Gregori, C. A. Puliafito, "Registration of high-density cross sectional images to the fundus image in spectral-domain ophthalmic optical coherence tomography," Optics Express **14**, 3368-3376 (2006). http://www.opticsinfobase.org/oe/abstract.cfm?URI=oe-14-8-3368.

[20] Srinivasan, V.J., T.H. Ko, M. Wojtkowski, M. Carvalho, A. Clermont, S.E. Bursell, Q.H. Song, J. Lem, J.S. Duker, J.S. Schuman, and J.G. Fujimoto. Noninvasive volumetric imaging and morphometry of the rodent retina with high-speed, ultrahigh-resolution optical coherence tomography. *Invest Ophthalmol Vis Sci*. 2006; **47**(12):5522-8.

[21] Ruggeri, M., H. Wehbe, S. Jiao, G. Gregori, M.E. Jockovich, A. Hackam, Y. Duan, and C.A. Puliafito. In vivo three-dimensional high-resolution imaging of rodent retina with spectral-domain optical coherence tomography. *Invest Ophthalmol Vis Sci*. 2007; **48**(4):1808-14.

[22] Kim, K.H., M. Puoris'haag, G.N. Maguluri, Y. Umino, K. Cusato, R.B. Barlow, and J.F. de Boer. Monitoring mouse retinal degeneration with high-resolution spectral-domain optical coherence tomography. *J Vis*. 2008; **8**(1):17 1-11.

[23] ANSI, *American National Standard for Safe Use of Lasers, ANSI Z 136.1-1993*. 1993, Orlando, Fla: The Laser Institute of America. 37-43.

[24] Sarunic, M.V., S. Asrani, and J.A. Izatt. Imaging the ocular anterior segment with real-time, full-range Fourier-domain optical coherence tomography. *Arch Ophthalmol*. 2008; **126**(4):537-42.

[25] Zawadzki, R.J., C. Leisser, R. Leitgeb, M. Pircher, and A.F. Fercher. *3D ophthalmic OCT with a refraction correction algorithm*. in *SPIE Biomedical Optics*. 2003. San Jose, CA.

[26] Xu J, Molday LL, Molday RS, Sarunic MV. In Vivo Imaging of the Mouse Model of X-Linked Juvenile Retinoschisis with Fourier Domain Optical Coherence Tomography. *Invest Ophthalmol Vis Sci* 2009;50:2989-2993.

[27] Weber, B.H., H. Schrewe, L.L. Molday, A. Gehrig, K.L. White, M.W. Seeliger, G.B. Jaissle, C. Friedburg, E. Tamm, and R.S. Molday. Inactivation of the murine X-linked juvenile retinoschisis gene, Rs1h, suggests a role of retinoschisin in retinal cell layer organization and synaptic structure*. Proc Natl Acad Sci U S A*. 2002; **99**(9):6222-7.

[28] Apushkin, M.A. and G.A. Fishman. Use of dorzolamide for patients with X-linked retinoschisis*. Retina*. 2006; **26**(7):741-5.

[29] Apushkin, M.A., G.A. Fishman, and M.J. Janowicz. Correlation of optical coherence tomography findings with visual acuity and macular lesions in patients with X-linked retinoschisis*. Ophthalmology*. 2005; **112**(3):495-501.

[30] Gerth, C., R.J. Zawadzki, J.S. Werner, and E. Heon. Retinal morphological changes of patients with X-linked retinoschisis evaluated by Fourier-domain optical coherence tomography*. Arch Ophthalmol*. 2008; **126**(6):807-11.

[31] Pease, M.E., McKinnon, S.J., Quigley, H.A., Kerrigan-Baumrind, L.A. & Zack, D.J. Obstructed axonal transport of BDNF and its receptor TrkB in experimental glaucoma. *Invest Ophthalmol Vis Sci* **41**, 764-774 (2000).

[32] Ko, M., Hu, D., Ritch, R. & SC, S. The combined effect of BDNF and a free radical scavanger in experimental glaucoma. *Invest. Ophtalmol. Vis. Sci.* **41**, 2967-2971 (2000).

[33] Martin, K.R*., et al.* Gene therapy with brain-derived neurotrophic factor as a protection: retinal ganglion cells in a rat glaucoma model. *Invest Ophthalmol Vis Sci* **44**, 4357-4365 (2003).

[34] Pease, M.E., McKinnon, S.J., Quigley, H.A., Kerrigan-Baumrind, L.A. & Zack, D.J. Obstructed axonal transport of BDNF and its receptor TrkB in experimental glaucoma. *Invest Ophthalmol Vis Sci* **41**, 764-774 (2000).

[35] Shi, Z., Birman, E. & Saragovi, H.U. Neurotrophic rationale in glaucoma: a TrkA agonist, but not NGF or a p75 antagonist, protects retinal ganglion cells in vivo. *Dev Neurobiol* **67**, 884-894 (2007).

[36] Lebrun-Julien, F., Morquette, B., Douillette, A., Saragovi, H.U. & Di Polo, A. Inhibition of p75(NTR) in glia potentiates TrkA-mediated survival of injured retinal ganglion cells. *Mol Cell Neurosci* **40**, 410-420 (2009).

[37] Shi, Z.*, et al.* alpha 2 macroglobulin is a mediator of retinal ganglion cell death in glaucoma. *J Biol Chem* (2008).

[38] Pernet, V. & Di Polo, A. Synergistic action of brain-derived neurotrophic factor and lens injury promotes retinal ganglion cell survival, but leads to optic nerve dystrophy in vivo. *Brain* **129**, 1014-1026 (2006).

[39] Zhi, Y.*, et al.* Different optic nerve injury sites result in different responses of retinal ganglion cells to brain-derived neurotrophic factor but not neurotrophin-4/5. *Brain Res* **1047**, 224-232 (2005).

[40] Jost D. Jonas, Xuan N. Nguyen, and Gottfried O. H. Naumann, "Parapapillary retinal vessel diameter in normal and glaucoma eyes. I. Morphometric data", Investigative Ophthalmology & Visual Science, Vol. 30, No. 7, July 1989

[41] Rohlich P, Szel A. Photoreceptor cells in the Xenopus retina. Microsc Res Tech 2000;50:327-337.

[42] Srinivasan, V.J., T.H. Ko, M. Wojtkowski, M. Carvalho, A. Clermont, S.E. Bursell, Q.H. Song, J. Lem, J.S. Duker, J.S. Schuman, and J.G. Fujimoto. Noninvasive volumetric imaging and morphometry of the rodent retina with high-speed, ultrahigh-resolution optical coherence tomography*. Invest Ophthalmol Vis Sci*. 2006; **47**(12):5522-8.

[43] Weber, B.H., H. Schrewe, L.L. Molday, A. Gehrig, K.L. White, M.W. Seeliger, G.B. Jaissle, C. Friedburg, E. Tamm, and R.S. Molday. Inactivation of the murine X-linked juvenile retinoschisis gene, Rs1h, suggests a role of

retinoschisin in retinal cell layer organization and synaptic structure. *Proc Natl Acad Sci U S A*. 2002; **99**(9):6222-7.

[44] Apushkin, M.A. and G.A. Fishman. Use of dorzolamide for patients with X-linked retinoschisis. *Retina*. 2006; **26**(7):741-5.

[45] Apushkin, M.A., G.A. Fishman, and M.J. Janowicz. Correlation of optical coherence tomography findings with visual acuity and macular lesions in patients with X-linked retinoschisis. *Ophthalmology*. 2005; **112**(3):495-501.

[46] Gerth, C., R.J. Zawadzki, J.S. Werner, and E. Heon. Retinal morphological changes of patients with X-linked retinoschisis evaluated by Fourier-domain optical coherence tomography. Arch Ophthalmol. 2008; 126(6):807-11.

[47] Lee DC, Xu J, Sarunic MV, Moritz OL. Fourier domain optical coherence tomography (FD-OCT) as a non-invasive means for in vivo detection of retinal degeneration in Xenopus laevis tadpoles. *Invest Ophthalmol Vis Sci* 2009; 0: iovs.09-4260v1

[48] Nieuwkoop PD, Faber J. *Normal table of Xenopus laevis (Daudin) : a systematical and chronological survey of the development from the fertilized egg till the end of metamorphosis*. New York: Garland Pub.; 1994:252 , 210 leaves of plates.

[49] Tam BM, Moritz OL. Dark rearing rescues P23H rhodopsin-induced retinal degeneration in a transgenic *Xenopus laevis* model of retinitis pigmentosa: a chromophore-dependent mechanism characterized by production of N-terminally truncated mutant rhodopsin. *J Neurosci* 2007;27:9043-9053.

[50] Tam BM, Moritz OL. Characterization of Rhodopsin P23H-Induced Retinal Degeneration in a *Xenopus laevis* Model of Retinitis Pigmentosa. *Invest Ophthalmol Vis Sci* 2006;47:3234-3241.

[51] Hamm LM, Tam BM, Moritz OL. Controlled rod cell ablation in transgenic *Xenopus laevis*. *Invest Ophthalmol Vis Sci* 2008.

[52] Robert H. Webb, George W. Hughes, and Francois C. Delori, "Confocal scanning laser ophthalmoscope," Appl. Opt. 26, 1492-1499 (1987).